Stony Brook University

Characterization of Defects in Bulk Sapphire Single Crystals

A Thesis Presented

by

Yu Yang

to

The Graduate School

in Partial Fulfillment of the

Requirements

for the Degree of

Master of Science

in

Materials Science and Engineering

Stony Brook University

December 2012

Stony Brook University

The Graduate School

Yu Yang

We, the thesis committee for the above candidate for the

Master of Science degree, hereby recommend

acceptance of this thesis.

Michael Dudley - Thesis Advisor
Professor, Materials Science and Engineering

Balaji Raghothamachar - Second Reader
Assistant Professor, Materials Science and Engineering

T. A. Venkatesh – Third Reader
Assistant Professor, Materials Science and Engineering

This thesis is accepted by the Graduate School

Charles Taber
Interim Dean of the Graduate School

Abstract

Defects would effect the optical properties and operation performances of sapphire single crystal material. Further understanding the defects structure and origins in sapphire plays a crucial role. This study is focusing on analyzing the structure of linear, 2D and 3D defects using the X-ray topography technique. Several other techniques such as etch pits method and X-ray reticulography are also employed to revealing the properties of dislocations and stress distribution around certain defect feature.

Table of Contents

List of Figures

Chapter 1. **Introduction**

1.1 Crystal structure of sapphire

Sapphire is the crystalline form of alumina (α-Al_2O_3) and has a rhombohedral crystal structure consisting of Al^{3+} cations and O^{2-} anions. The structure of sapphire as shown in Figure 1.1 can be described as O^{2-} anions in the form of solid spheres in a closed-packing hexagonal arrangement. The Al^{3+} cations are located in the octahedral sites formed by as 6 O^{2-} anions. To satisfy the stoichiometric requirements, only two-thirds of the sites are filled. The coordination number of Al^{3+} is 6 and for O^{2-} is 4. Both Al and O have different but repeating layers of spatial arrangements along the third axis defined by O. The Al sub-lattice repeats every 3 layers, the hexagonal close packed O sub-lattice repeats every 2 layers, so that a complete cycle for ordered repeating contains 6 O layers, and 6 Al layers respectively. The distortion of the O sublattice leads by the certain radii of Al cation (0.57Å) compared to the O ion (1.40), and the asymmetric distribution of the Al atoms around the O atoms creates a pseudo-hexagonal structure which slightly deviates from the ideal close packed hexagonal structure, resulting in a *c/a* ratio of 1.58 (compared to 1.63 for the ideal one). More details on the bonding can be obtained from the images in Fig.1.2 Along the c-axis, the 3 shorter distances of Al-O bonds are equal to 1.86 Å, the other 3 bigger ones are 1.97Å, and they interchange in different pairs and different intermediate layers. The Al-Al layer spacing is 2.65A and the O-O layers spacing is 2.49 or 2.87 respectively. Also, along the c-axis, the triangles composed of 3 O ions parallel to each other in neighboring layers are rotated 64.3º compare to the 60º in ideal condition. The approximate hexagonal structure parameter for sapphire is $a = b = 4.759213$ÅA; $c = 12.9915867$Å at 295.65K.

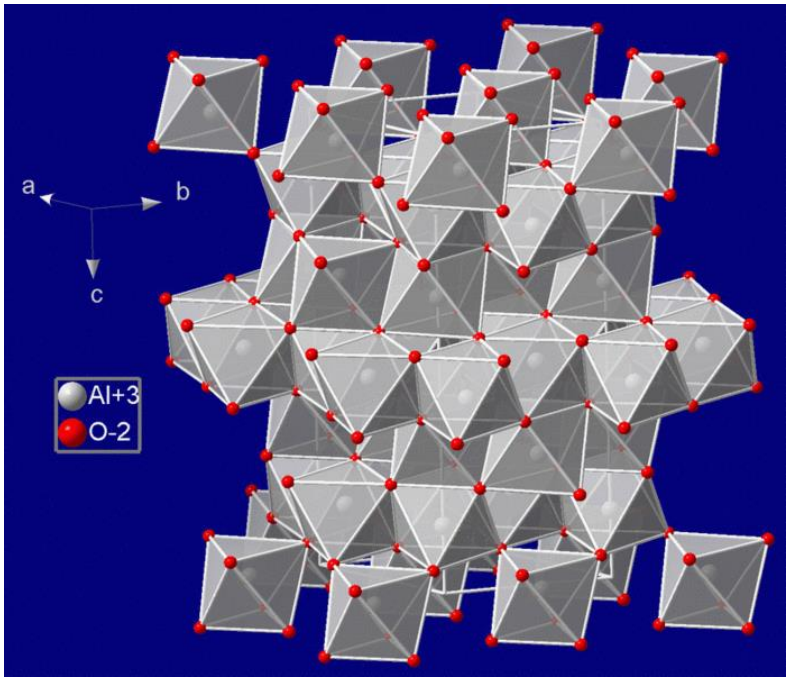

Figure 1.1. Crystal structure of sapphire[1]

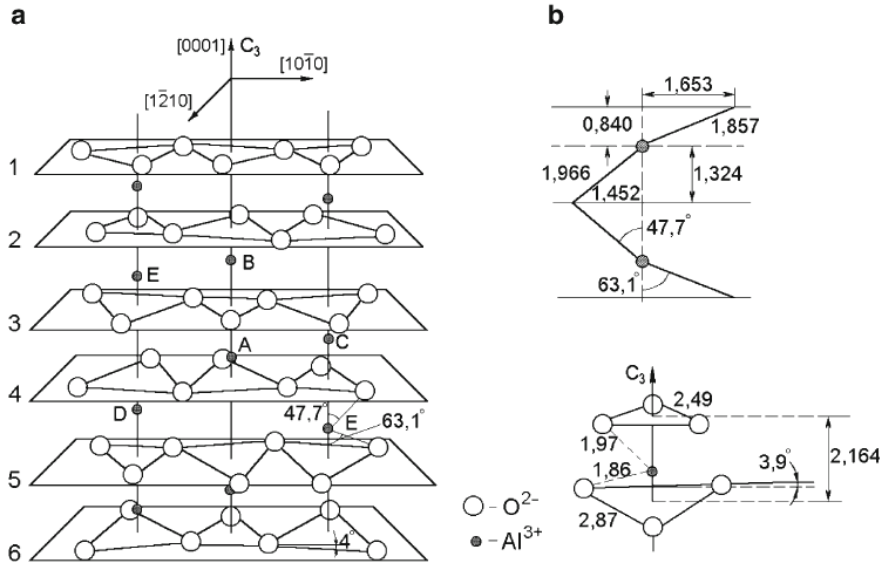

Figure 1.2. (a) schematic of arrangement of Al^{3+} cations and O^{2-} ions layers; (b) the distance between Al^{3+} and O^{2-} ; (c) the position of Al^{3+} cation surrounded by O^{2-} ions

According explained above, customarily we treat alpha-Al_2O_3 as a pseudo-hexagonal structure during defect analysis. For further understanding the mechanisms of defect formation in sapphire crystals, the properties of hexagonal structure, especially possible types of slip systems needs to be explored. [2]

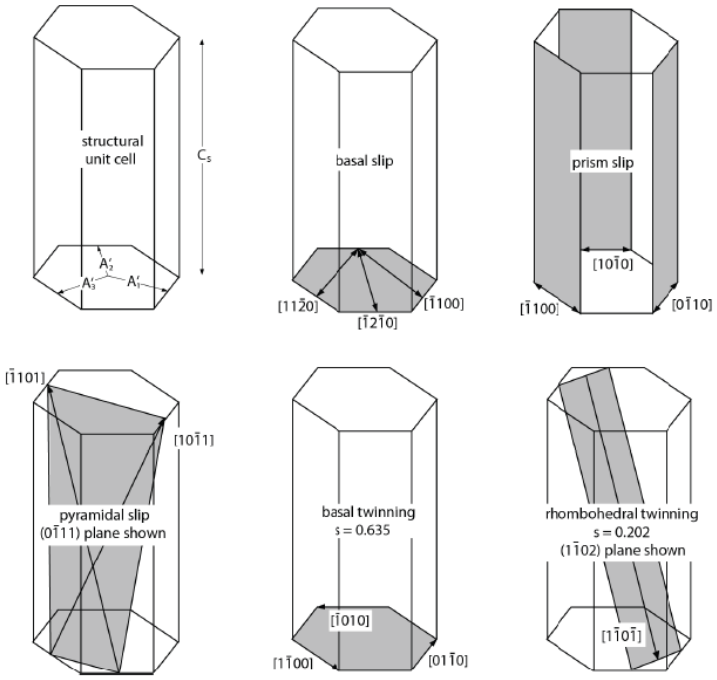

Figure 1.3. Sapphire unit cell (a) and deformation systems: (b) Basal slip (0001) <11-20>; (c) Prism slip {10-10} <1-210>; (d) Pyramidal slip {1-101} on <10-11> ; (e) Basal twinning; (f) Rhombohedral twinning.

1.1.1 Possible slip systems and defects

Sapphire, as a pseudo-hexagonal structure, has the basal slip system as the predominant deformation mechanism. Additionally, prism slip and pyramidal slip have also been reported[3]. Basal and rhombohedral deformation twinning is also observed in sapphire as shown in Fig. 1.3.

The types of crystal defects can be broadly classified into four categories:

1. Point defects, which can be defined as an missing atom (vacancy) or substitution by impurity atoms;
2. Linear defects, i.e. dislocations;
3. Planar defects, which can be described as an abrupt change of the organized crystal arrangement between the homogenous materials in two dimension form e.g. grain boundaries, stacking faults and twins;
4. Bulk defects, which occurs in a much bigger scale, such as large amounts of vacancies or atoms clustering together to form voids or impurities. And also the cracks and secondary phases.[4]

1.2 Growth method

1.2.1 Czochralski (CZ) process

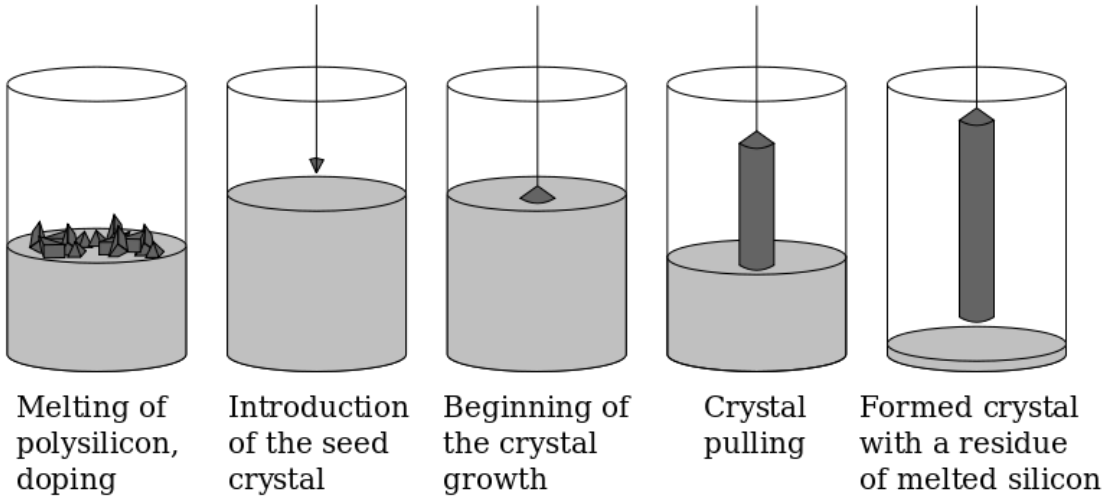

Figure 1.4. A simplified Czochralski process (shown for silicon growth; same procedure for sapphire).

Before the growth process begins, the seed material is placed in a molybdenum crucible located in a crystal growth chamber. The gas in the chamber has to be evacuated at first, filling it with inert gas next. This would prevent lowering crystal quality through introduction of contamination products created by the reaction between atmosphere gas and the charge material. A slim seed crystal with precise orientation is dipped into molten solution, and slowly pulled upwards and rotated at a controlled rate simultaneously. The seed and the crucible rotate in different directiond. Crystal diameter is increased gradually during every seed rotation cycle until it reaches the required size. The whole process of CZ growth process is illustrated in Fig. 1.4.

The controlling factors, such as the temperature gradients, rate of pulling and speed of rotation, are decisive, which make it possible to extract a large, single, cylindrical crystal from the melt. The common parameters are rotation rates up to 30rpm. The speed of pulling the seed out of the melt at 6-25mm/hr for a growth time that can reach up to 8-10 weeks. This technique is the commercial way to grow large diameter sapphire boules with superior optical properties. Czochralski growth technique can achieve the size 150mm in diameter and 250mm in length.[5,6]

1.2.2 Verneuil process

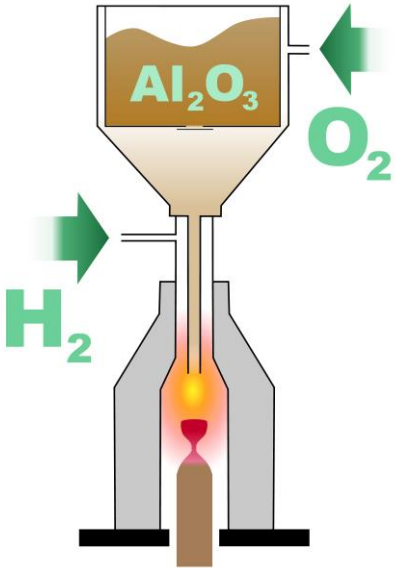

Figure 1.5. A simplified Verneuil process

In this technique, finely powdered charging material is placed in a hopper at first as illustrated in Fig. 1.5. A mechanical hammer is employed later for tapping the powder down through a tube while O_2 gas is passed through the Al_2O_3 melted powder. H_2 gas is supplied into the bottom of the crucible and the charge is heated to 2000º. Initial powder built up a conical pile as the results of the melted hot particles which finally sintered together to form the rigid "sinter cone". The upper tip of the cone becomes molten when the cone tip achieved sufficient sharpness. Gradually, the new powder landing on would melt and enlarge the crystal to form the boule. The controlling factor for this method is also the flame temperature, which should be no higher than the fusion temperature. Care should be taken to keep the molten product at the same part of flame, and the contact point area should be reduced as small as possible. For Verneuil method, the most significant advantage is this is the most commercial method to grow large size sapphire single crystal comparably. However the primary disadvantage is that this method does not meet the quality requirement for electronic and optical applications.[7,8]

1.2.3 Kyropoulos Method:

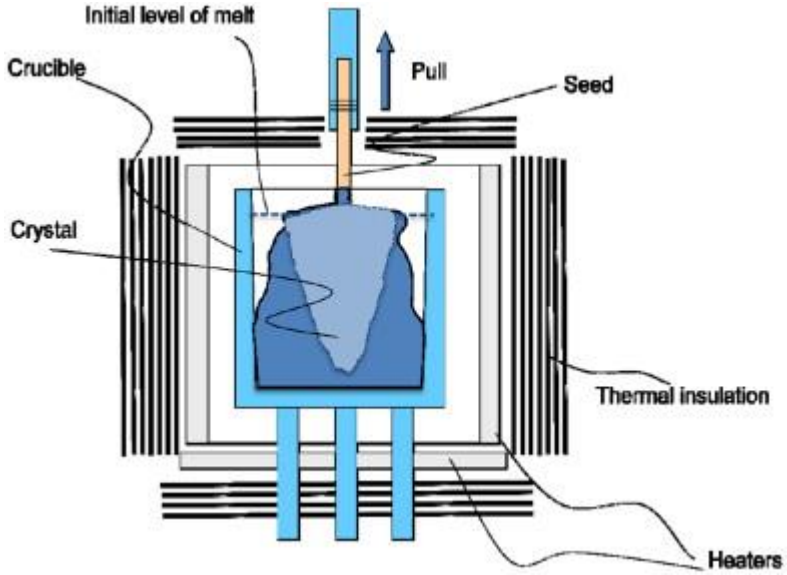

Figure 1.6. A simplified Kyropoulos process

Pure alumina powder is placed in crucible, which is located in an enclosed chamber (see Fig. 1.6). The alumina powder is finally turned into the melt by using the resistive heating technique. Seed crystal at the end of the water cooling rod should be attached at its top and gradually lowered into the melt. A suitable thermal environment designed to allow only the top of the powder-seed interface to melt. Then the seed is drawn back slowly (velocity slower than the crystallization speed). The main characteristics of this method is the very low vertical temperature gradient employed for growth. Pulling operation only employed at the beginning of the seeding process. Moreover, no rotation is needed in this method. The charging material fills almost the whole crucible and freezing occurs from the top to its bottom during crystallization. Major advantage of this method is it is ideal for growing materials with low thermal conductivity and high level of thermal expansion rate. With the strictly controlled thermal gradient, high optical quality sapphire boule with low defect density and large size can be produced using this method.[9,10]

1.2.4 Heat Exchanger Method (HEM)

The furnace mainly consists of a water cooled heat zone chamber and a helium gas coolant tube, which is illustrated in fig. 1.7. The heat zone chamber is located in the center of the whole furnace and wrapped up by the vertical cylindrical water chamber for protection. The seed crystal cooled by the coolant gas tube is placed in the bottom of the heat zone and was connected to the molten pure material powder filled in the chamber. The crucible can be filled and evacuate by changing the pressure through inflating and pumping gas. And the charging element powder can be melted by the heat supplied by the graphite resistance heater. To prevent the seed crystal from the melting at the beginning of the crystallization process, only the minimum flow of coolant gas is needed. After part of the seed crystal melted, higher flow of coolant gas charges to initiate the crystallization from the bottom to the top. The whole process is maintained at a constant temperature. When the growth process is completed, lower temperature and flow of coolant gas is maintained to anneal the boule.

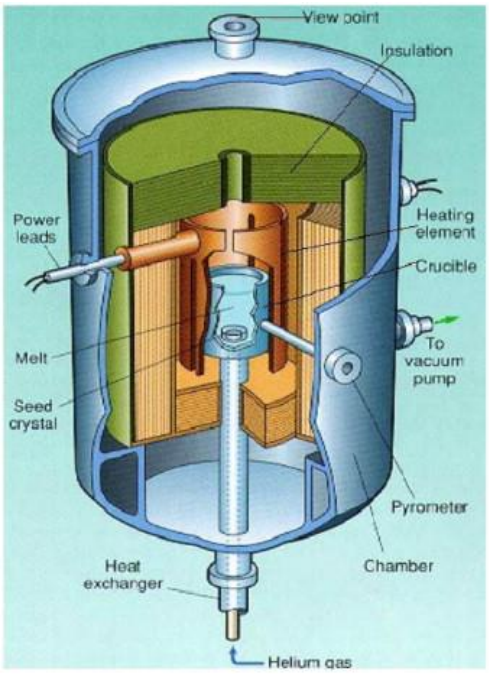

Figure 1.7. A schematic of the HEM furnace

For HEM, large diameter crystal can be obtained through this method; At least 95 percent of the melt can be converted to the high quality crystal; And it also have a great potential and capable for growing the laser crystals cause the better laser performance results from the high quality.[10,11]

1.2.5 Temperature Gradient Technique (TGT)

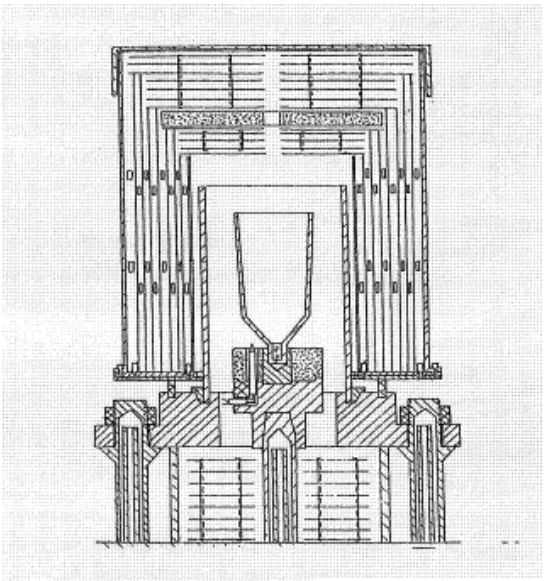

Figure 1.8. A schematic of the TGT furnace

The crucible made of Molybdenum is positioned in the center of the whole furnace which is surrounded by a cylindrical shaped graphite heating element pierced with holes in certain pattern,

which is illustrated in Fig.1.8. The graphite heating element heats the crucible through an electric circuit which has a linear resistance. The whole heater is supported by the graphite electrodes, which is cooled by the tubes filled with cold water passing through it. The tubes also connect to the bottom of the crucible where the seed is located, so that the hot water flow can be cycled for additional heating. The temperature controlling procedure at different parts of the crucible employs different mechanisms. For the upper part, the temperature gradient is maintained by the linear resistances from the graphite heater; the lower part heated by the coolant water which extracted the heat from the graphite electrodes when passing through them. And the temperature surround the seed is also influenced by the heat conductivity of the water cooled center rod.

For TGT, the most typical feature is all the procedures are operating under static condition. Temperature changes in a designed rate in the crucible by the very precise temperature controller. When the crystallization begins, the water flow should be stable to make sure the solid and the liquid interface advances upwards with a constant velocity. Crystals grown by TGT have lower dislocation density and less scattering - shows a great advantage for growing laser material.[12]

1.3 Application

Sapphire is normally used as substrates for growing compounds for light emitting diodes (LEDs), or infrared (IR) detectors for growing mercury cadmium tellurium, GaAs wafer carriers and the microwave integrated circuits.

In aerospace field, sapphire is used for conventional windows and dome shapes which can take the place of softer and more fragile IR transmitting materials due to its better performance in wide transmission range under the corrosive, high temperature conditions. And it also can be employed as infrared countermeasures lamps due to its high temperature resistance with broad spectral range.

In analytical field, sapphire is suitable for applications which demand the materials with combination of properties such as ultraviolet and infrared transmission as well as capability to operate under high temperature, high pressure even chemical erosion. It could be used as nuclear magnetic resonance tubes, taking place of the conventional glass or quartz materials, which should undergo a very high pressure environment condition; It could also be used as digestion cells like sheaths and liners while the hydrofluoric acid is used during sample preparation. And it also could be used in analytical chemistry, instead of quartzware due to its advance in supplying good UV transmission while more durable and clean in spectroscopy, ICAP and other systems.

In medical field, sapphire could be used as surgical tips for laser transmission and contacting body fluids in different surgical laser applications. It could also be made as very thin knives, which could offer the perfect cut edge which giving distortion free sections down to the 10μm level.

Sapphire is most widely used in optical field due to its UV and IR properties combined with its durability in high temperature environment. It could be used for high brightness illumination windows, for it can bear an extremely high heat and offer widest spectral transmission at the same time, such as sapphire rods for light guides. Also due to its high optical property, it could be used as optical components like lenses, prisms and other types of laser or infrared optical. In watch industry, different shapes of the scratchproof sapphire crystal watch glasses are in the most urgent demand due to its hardness.[13]

Chapter 2. **Experimental techniques**

2.1 X-ray topography

Because of the increasing demand for high quality single crystal in industrial, the nondestructive X- ray diffraction imaging technique, X-ray topography due to inherent advantages, is broadly used in detecting defects in single crystals. X-ray diffraction is the phenomenon that different crystal planes can scatter corresponding length of waves which reinforce or extinct each other to create different intensities and finally forms the diffraction pattern. The selecting rule is satisfied for the Bragg Law:

$$\lambda = 2d\sin\theta$$

where λ here is the X-ray wavelength, d is the inter spacing of diffracting planes, and θ is the angle between the incident beam and the diffraction planes, which is normally called Bragg angle.

X-ray topography is an imaging technique based upon Bragg Law. Information of intensity distribution is recorded in two-dimension on positive film. Intensity variation in those multiple diffraction spots is a function of position in crystal. Local diffraction contrast of defects is the given result of intensity difference between distortion surrounding the defect area and the surrounding perfect regions. Normally specific contrast could be identified which is generated by particular defect type correspondingly. Detailed information of defects could be analyzed by interpreting the variations of contrast.

In general, contrast is induced by two mechanisms below:

(a) Orientation contrast, as the name implies, is caused by misorientation of lattice planes in crystal. The inhomogeneous intensity is the results of the convergence or divergence of the x-ray beam locally. The mechanism is purely geometrical as shown in Fig.2.1 below. Separation of exit beam paths produces white contrast, while overlap produces dark contrast. Defects exhibiting orientation contrast are normally grain boundary, subgrains, and twins.

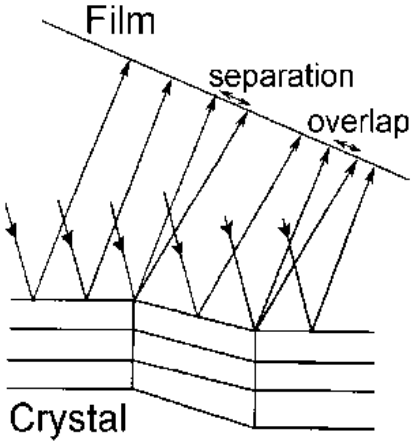

Figure 2.1. Schematic showing the mechanism of orientation contrast

(b) Extinction contrast is the result of different scattering power around defect from the rest of the crystal, which is normally used for understanding dislocation contrast in topography. Three types of images could be observed due to different types of extinction contrast:

(i) Direct dislocation image: This type of image is recorded under low absorption condition where the dislocation core has stronger contrast than surrounding areas.

(ii) Dynamical dislocation image: This type of image is recorded under high absorption condition where the dislocation core shows in white contrast due to Borrmann effect.

(iii) Intermediary dislocation image: This type of image is recorded under intermediary absorption condition where the dislocation shows as a bead-line due to the combination of all the three mechanisms.

For further understanding the origins of dislocations, quantitative imformtaion such as dislocation line direction and Burgers vector should be determined. The image of the dislocation line could be simply treated as geometric projection, and its three-dimension morphology could be found by comparing different images recorded in different geometric settings. Qualitative analysis could be employed for understanding how the diffraction vector (**g**) and Burgers vector (**b**) affect the contrast. Generally, cancellation of contrast occurs when:

For screw dislocations**, g.b** = 0

For edge and mixed dislocations, **g. b** = 0 and **g.b**×**l** = 0,

Where the **g, b, l** are the diffraction plane normal vector, Burgers vector, and the dislocation line direction respectively.

All the X-ray topography experiments were carried out using the synchrotron white beam X-ray source, which is located at National Synchrotron Light Source, beamline X-19C hutch at Brookhaven National Laboratory. Mainly four geometries are employed for recording depending on different samples and experimental purposes.

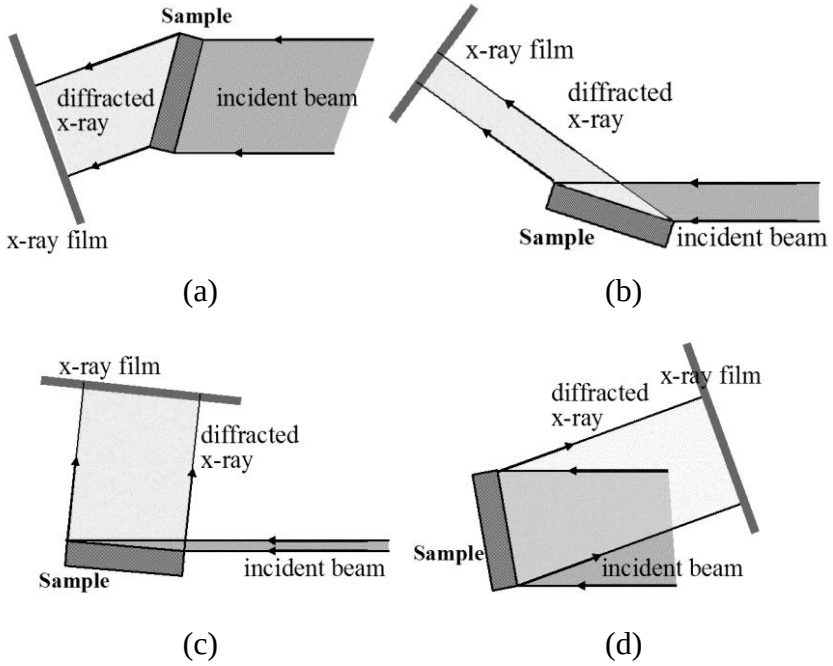

Figure 2.2. X-ray topography imaging geometries, (a) transmission, (b) reflection, (c) grazing, (d) back-reflection

Fig.2.2 (a) is the transmission geometry, which is normally used for thin samples where the whole volume of defects could be recorded due to the sufficient X-ray penetration. (b) is the reflection geometry, which is employed for thick crystal commonly, and only the surface defect condition can be recorded. (c) is the grazing geometry which is only sensitive for those defects at low penetration depths. (d) is the back reflection geometry, which is normally used for determining the crystal orientation.[14]

2.2 X-ray reticulography

X-ray reticulography is an applied technique based upon the X-ray topography, whose operation is similar as single crystal Laue topography, but capable of quantifying misorientations in crystal lattice. Without measuring the lattice parameter change and the angular sharpness reflection, mapping the crystal misorientations in the topograph could be more easily achieved. The experimental setup shown in the Fig.2.2 below.

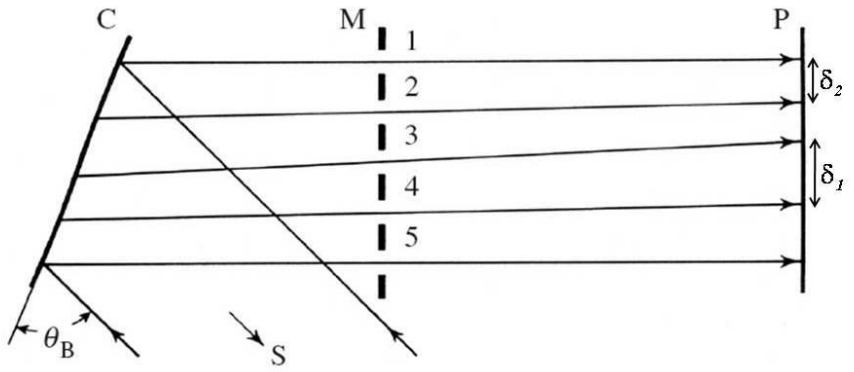

Figure 2.3. Schematic of experimental arrangement for X-ray reticulography

A fine-scale grid which can absorb X-ray is placed in the paths of the entrance or exit beams, which can split the area-filling X-ray beams into some identifiable microbeams. Here the M represents the absorbing grid, C is the specimen, S is the X-ray source, and P is the positive film. The un-uniform spacing on recording image indicates the corresponding local distortion in crystal indirectly by tracing the shifts of exit microbeams paths. Position of the reference point projected represents the stress condition of different lattice planes reflecting it. Extent of distortion could be different in different diffraction plane at the same position in crystal. [15]

More details for this technique are explained in section 4.2.

2.3 Chemical Etching

Nowadays, several techniques are utilized in revealing the existence and detection of dislocation properties. Although there are significant advantages in using synchrotron X-ray topography technique, like more sensitivity to dislocations and additional information, etching method is probably the most simplest and convenient way to detect the dislocations in crystal, which makes it valuable for further understanding.

For sapphire molten potassium hydroxide (KOH) is commonly used to etch and reveal dislocation defects. The etching procedure for c-plane and m-plane oriented samples varies slightly.

1. KOH etching of c-plane sapphire crystal

Heat the pure KOH in the Ni crucible until it is in molten state. Sapphire wafers are placed in this crucible containing molten KOH. Care should be taken that the whole sample is immersed in molten KOH for 1.5 hour. This process results in etching of the areas where there is high stress due to dislocations, etch pits corresponding to dislocations are formed. Following this the sample is cleaned using acetone and etch pits are observed using Nikon optical microscope. Some examples of this observation is shown in fig. 3.11, dislocations corresponding to the number of etch pits also is calculated.

2. KOH etching of m-plane sapphire crystal

For m-plane sample, same procedures for etching is carried out as for the c-plane sample, however the immersion in molten KOH was for a different duration. For m-plane samples, it takes four hours to reveal well-defined dislocation etch pits patterns.

2.4 Optical Microscopy

Using Nomarski optical contrast microscopy on a Nikon Eclipse 600W POL microscope, the surface morphology of samples was examined and compared with corresponding x-ray topographs. This helps in separating contrast features arising from surface artifacts caused by polishing or other processing from contrast features due to lattice defects. Surface of a single crystal can also sometimes reveal crystallographic information such as the nature of growth facets and steps. Optical microscopy is also used to measure study etch pit patterns produced by chemical etching.

Chapter 3. **Defects in sapphire wafers and axial slices**

3.1 Edge dislocations

In the pseudo-hexagonal crystal structure of alpha- Al_2O_3, typical defects related with the three slip systems: (0001)1/3<11-20> basal plane slip, (1-100){11-20} prism plane slip, and 1/3<10-11>{10-12} pyramidal plane slip have been reported so far. It is a well-known fact that the basal slip system is the main slip system due to lower critical shear stress compared to the other two, and which also makes it energetically more favorable for the defects to form at elevated temperatures.

Fig. 3.2 shows a 11-20 reflection imaged using transmission X-ray topography geometry (Fig. 3.1) from a m-cut sapphire sample. In this transmission geometry the sample is scanned across the X-ray beam with the film holder moving together with the sample as shown below.

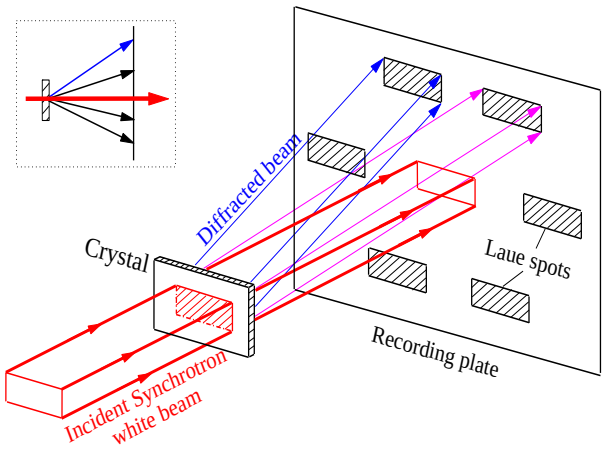

Figure 3.1. Schematic of the transmission geometry for recording topographs

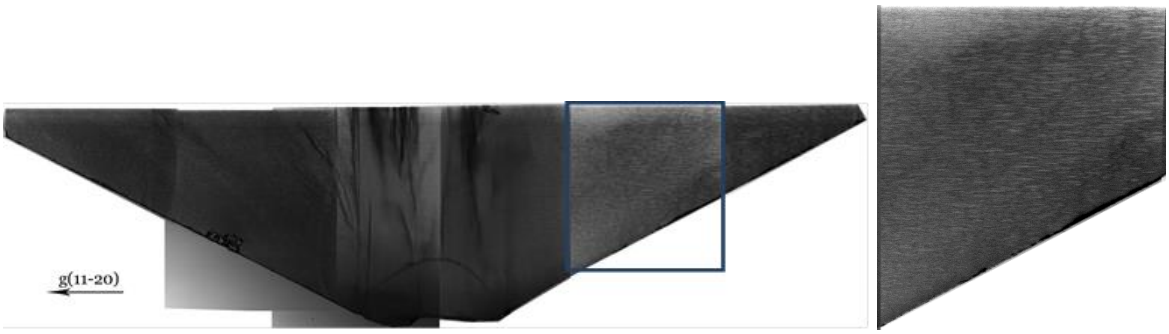

Figure 3.2. Transmission X-ray topograph (g = 11-20) recorded from a m-plane sapphire wafer showing the BPDs (see inset for high magnification topograph

On the 11-20 reflection, the commonly expected dislocation types, 1/3<11-20> can be observed due to relatively strong contrast based upon the **g.b** analysis. In this experiment, all the defects projections are perpendicular to the growth direction, which indicates all the dislocations are basal plane dislocations (BPDs), whose geometric alignments should be represented as some

horizontal lines just as the Fig. 3.1 shows. A selected region in this recorded topograph is enlarged in Fig.3.1 (b), which gives a clearer illustration.

Furthermore from all the studies done so far it appears that the most commonly observed BPDs are edge type dislocations. The is demonstrated in the X-ray topograph of a 2-inch diameter wafer (400 microns thick). Synchrotron white beam X-ray topography is used to record each of the three {1-100} type and {11-20} type reflections using the transmission scanning geometry. A high magnification region is analyzed in more detail as shown in Fig.3.3. By simple observation we can clearly notice that the dislocation lines aligning along <01-10> directions are invisible in the corresponding 0-110 reflections. Based on the extinction contrast analysis, in case of $\mathbf{g \cdot b = 0}$ & $\mathbf{g \cdot b \times l = 0}$ dislocation lines are totally out of contrast or exhibit weak contrast, we can confirm that those dislocations are pure edge dislocations with Burgers vector direction along <2-1-10>. Similarly, all the parallel dislocation lines distributed around the periphery are edge dislocations, and they move towards the center of the sample along <1-100> directions, forming a hexagonal pattern shown in Fig. 3.4. Several mixed dislocations are located in the center of the sample but the density is quite low compared to pure edge type BPDs. These edge-type BPDs are nucleated at high temperatures.

This sample studied is a representative example for dominant pure edge dislocation that appear in sapphire materials, which might have nucleated in high density at temperature below the melting point during crystal growth. Along with these dislocations other interesting features and defects are also observed in sapphire and are explained in details below.

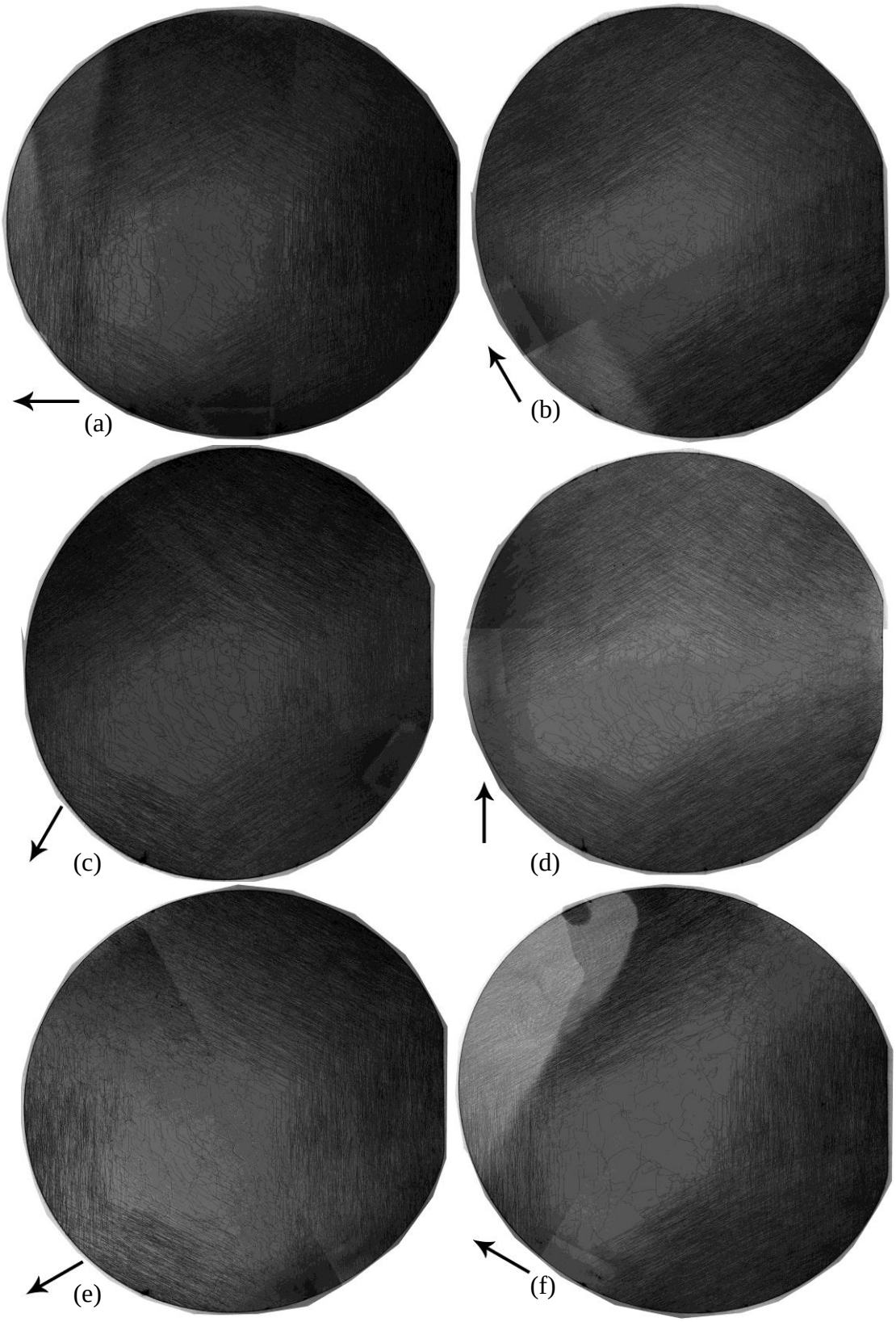

Figure 3.3. Transmission topographs recorded from a 2-inch sapphire wafer. (a) -1-120; (b) -2110; (c) 1-210; (d) -1100; (e) 0-110; (f) -1010.

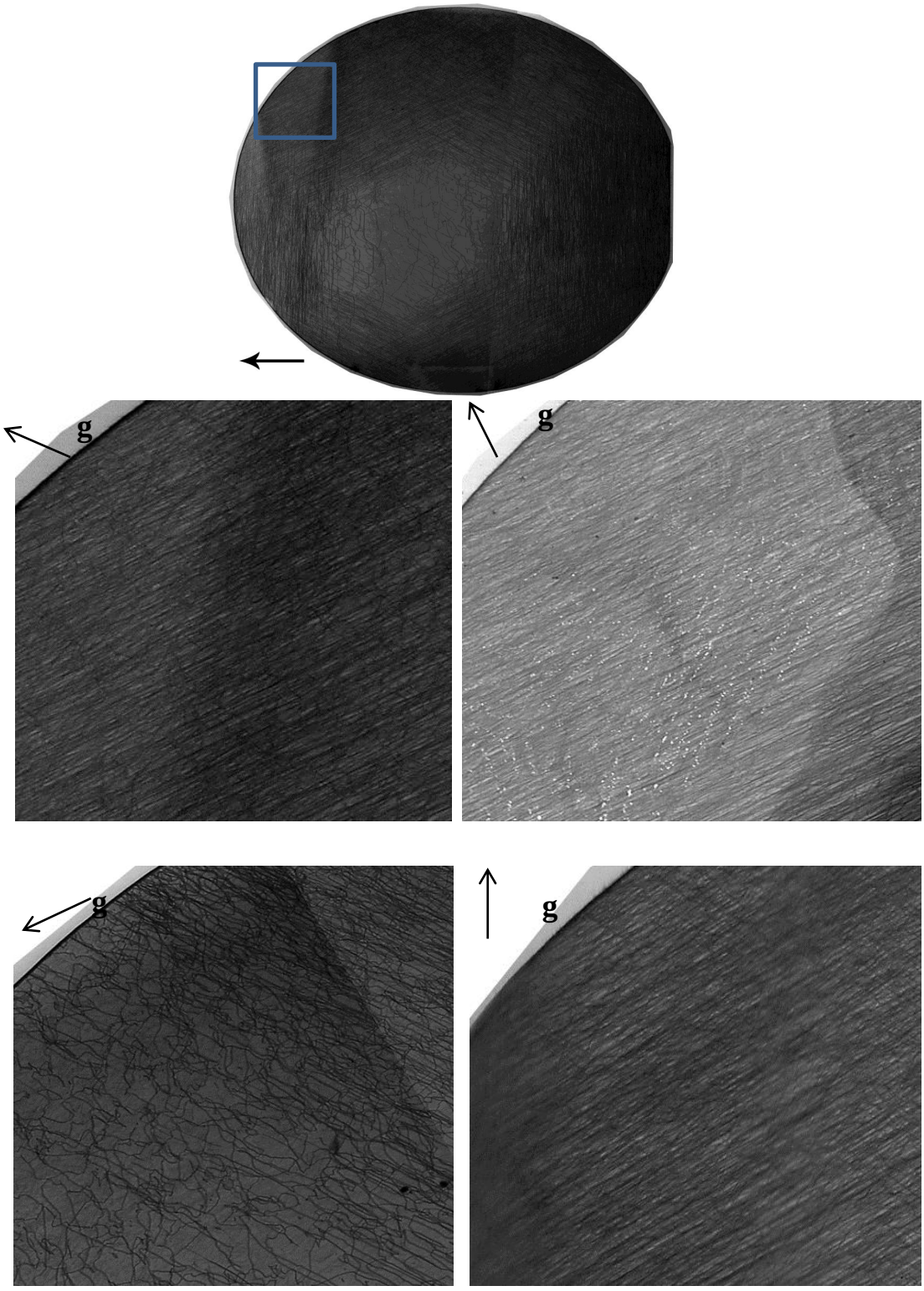

Figure 3.4. High magnification topographs from a selected region of a 2-inch wafer showing the extinction of edge dislocations on the <10-10>

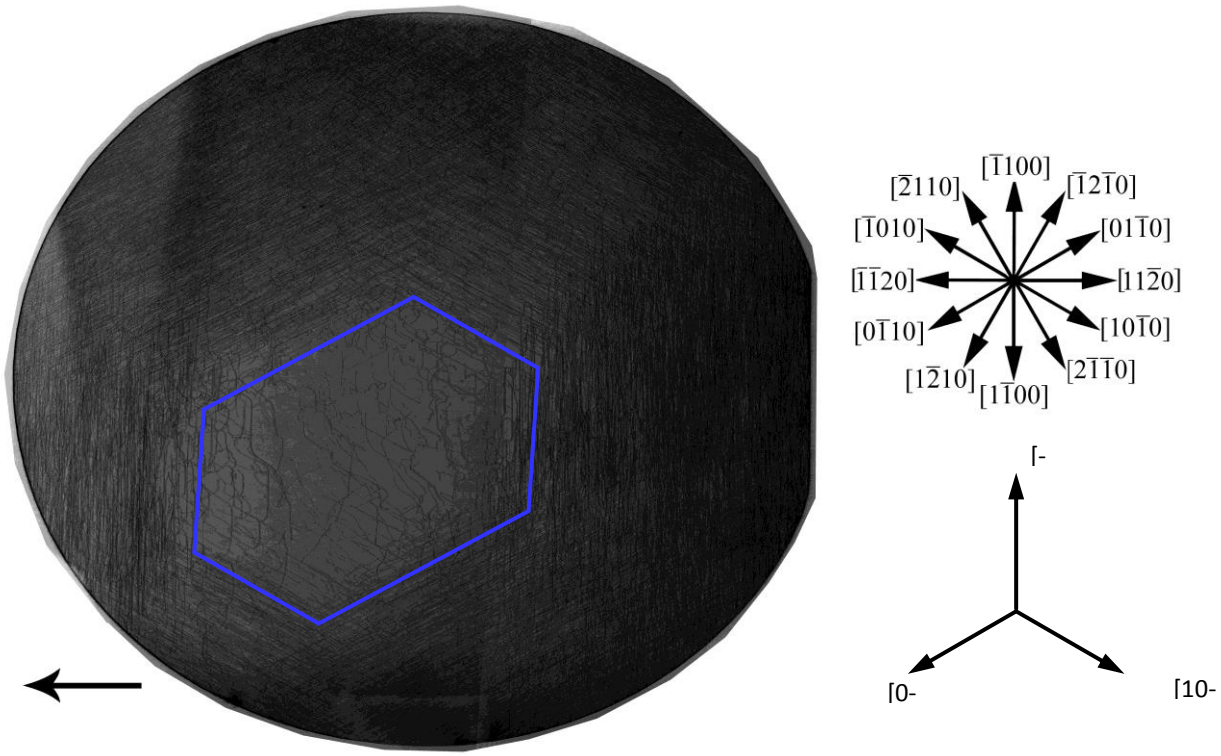

Figure 3.5. Dislocation lines arranged parallel to <1-100> direction

3.2 Helical dislocations

Many helical dislocations are observed near the central region of the same sample shown in Fig.3.6 (a). The areas are highlighted with blue squares. The formation of helical dislocations is a combination of three factors: dislocation line with screw component, pinning ends and availability of point defects at elevated temperatures to facilitate climb. Fig.3.7 shows the helix formation process in further detail: A straight dislocation line with a Burgers vector perpendicular to PN plane is growing into a curved shape lying in a cylinder flake whose axis is parallel to **b**, if two ends of the dislocation line are pinned. Further changes will happen while the dislocation climb and glide on this cylinder. Eventually the projection of the dislocation on PN will be a group of spirals shown in the diagram and therefore in this way a helical dislocation is formed.

In this specimen, two areas containing helices are magnified in Fig.3.6 (b)-(e) and (f)-(i). Fig 3.6(b) shows a complete helix which located in Area 1. However in Area 2, only part of the helical dislocation is shown in the sample, which means some parts have been cut off. The contrasts of both of these helices disappear in the 0-110 reflection, indicating that the Burgers vectors for those two helixes are along [2-1-10] direction and also parallel to their central axis. In general, Burgers vector of all the helical dislocations found from the samples in this study is along <11-20>.

An interesting reaction between two helices is also observed, which leaves a series of parallel dislocation loops behind. This phenomenon has also been found in the same specimen discussed above, which is located in Area 3 marked in Fig.3.6 (a).

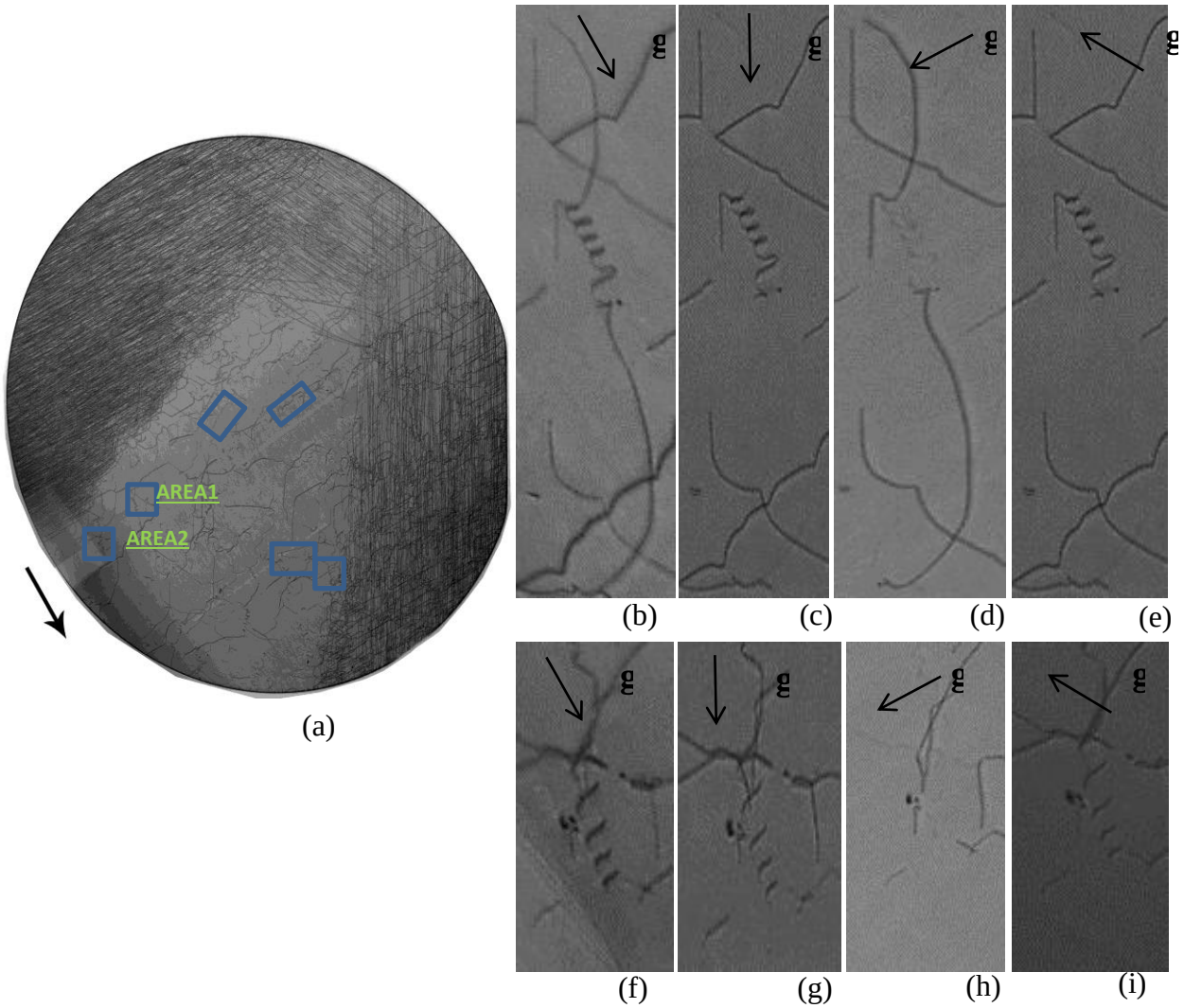

Figure 3.6. (a) Areas containing helices are marked as squares in 2-1-10 reflection; Area one contains a complete helix feature. Enlarged images of topograph from area one recorded in transmission geometry in (a) 2-1-10, (b) 1-100, (c) 0-110, and (d) -1010 reflections. Area two contains a partial helix feature which is cut by sample surface. Enlarged images of topograph from area two recorded in transmission geometry in (f) 2-1-10, (g) 1-100, (h) 0-110, and (i) -1010 reflections.

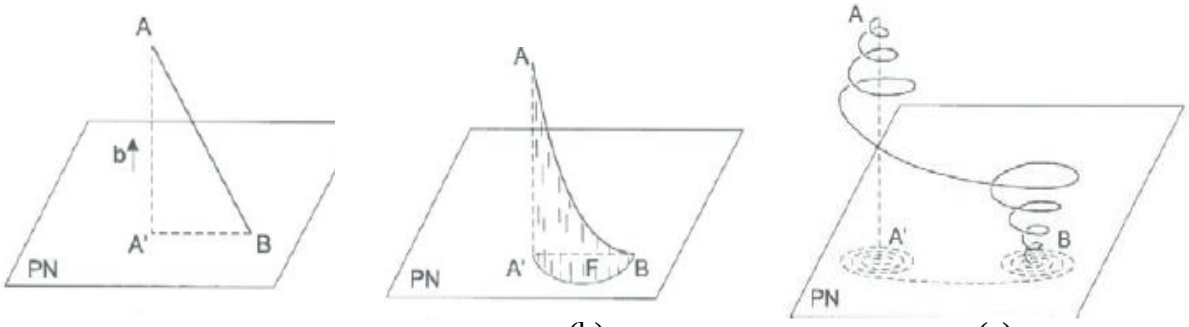

(a) (b) (c)

Figure 3.7. Helical dislocation forming process: (a) Burgers vector of a straight dislocation line AB is perpendicular to the projection plane PN. The dislocation is pinned in two ends. (b) AB dislocation line is growing into a curved shape lying in a cylinder flake whose axis is parallel to **b**. (c) A group of spirals forms in the end due to the dislocation line gradually climbs and glides along the cylinder. [16]

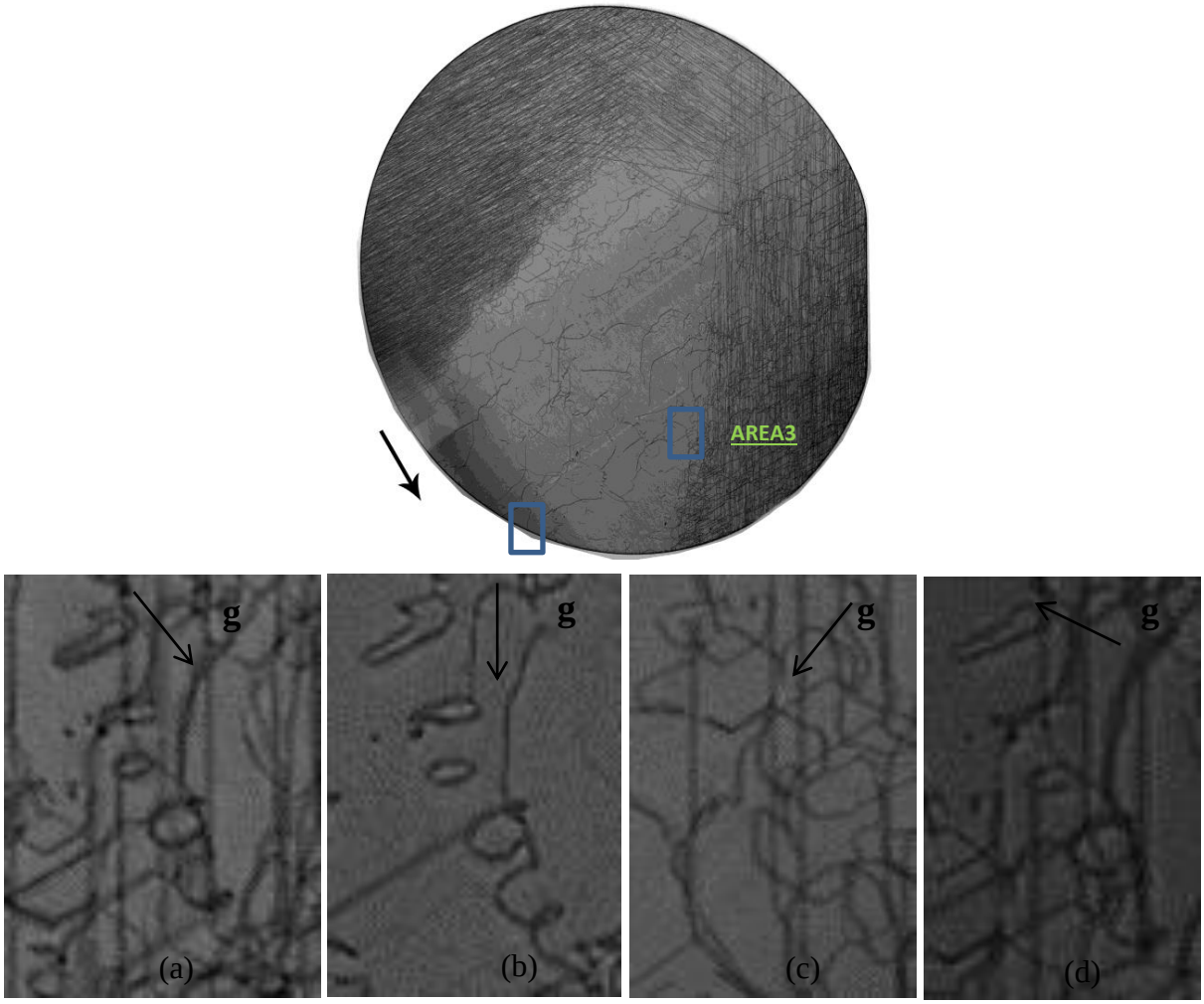

Figure 3.8. (a) Areas containing parallel loops are marked as squares in 2-1-10 reflection; Topograph images recorded in transmission geometry from Area3 are enlarged in (a) 2-1-10, (b) 1-100, (c) 0-110, and (d) -1010 reflections.

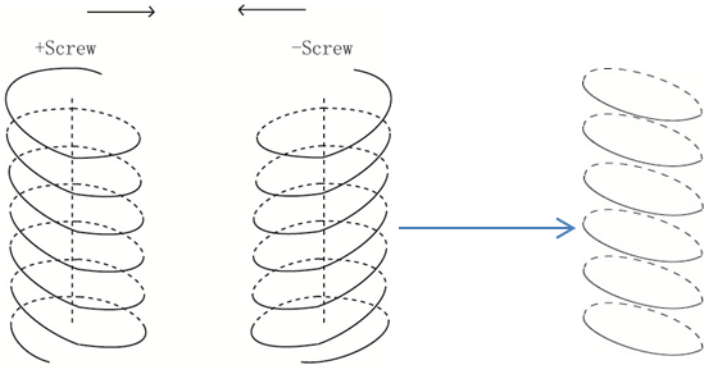

Figure 3.9. Illustration of two opposite sign helical dislocations forming a series of parallel edge dislocation loops due to the annihilation of the opposite sign dislocation segments.

The mechanism for formation of the series of parallel loops is as follows. An annihilation process, shown in Fig.3.9, happens when two helical dislocations with opposite signs coming across each other after which the group of parallel loops is left behind.

The example found in Area 3 is enlarged in Fig.3.8 (a)-(d). Loops disappears in 0-110 reflection, indicating that the Burgers vector is along [2-1-10]direction, aligned to the axis of the loops.[16]

3.3 Dislocation loops

Besides the helical dislocations, dislocation loops are found in the same sapphire wafer we analyzed above. High magnification images of the loops for the six basic reflections are shown in Fig.3.10 below. In each image the segment of dislocation loop tangential to the **g** vector are weak in but completely disappears only in the 2-1-10 reflection. This satisfies both the criteria simultaneously i.e. **g.b** = 0 and **g.b**× **l** = 0. Therefore we can infer that this loop is 1/3<1-101> type, and the Burgers vector in this particular case is aligned to be 1/3[1-101]. The illustration for contrast analysis is shown in Fig.3.11.

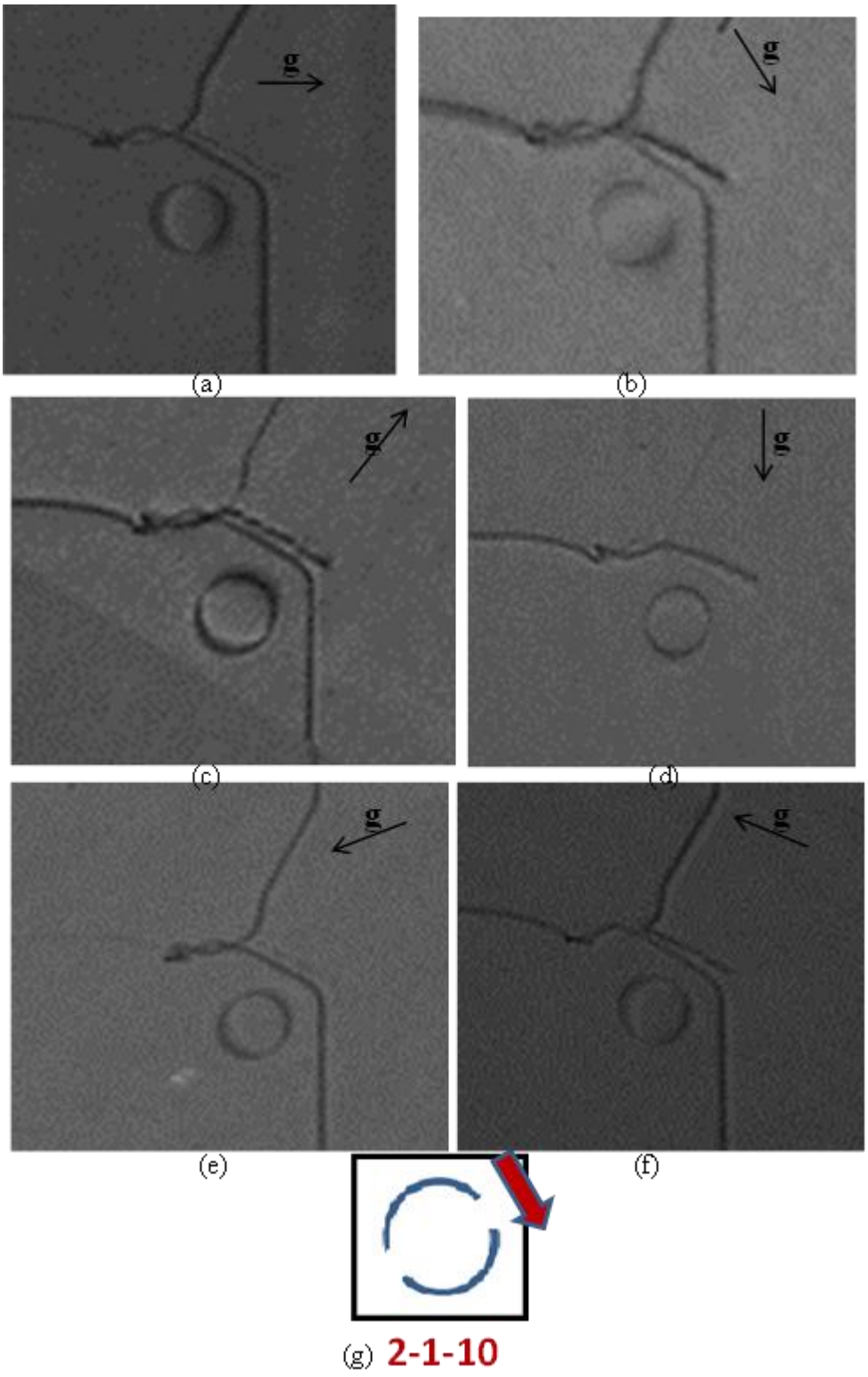

Figure 3.10. Enlarged images of topograph containing loop dislocation feature are recorded in transmission geometry in (a) 11-20, (b) 2-1-10, (c) -12-10, (d) 1-100, (e) 0-110, and (f) -1010 reflections. Segment lines parallel to **g** is in weaker contrast compare to the other part of the dislocation loop in every reflection but totally invisible in (2-1-10) reflection. An illustration in (g) represents this phenomenon more clearly

Mainly two types of mechanisms are involved in forming the dislocation loops:

1. Interstitial loops

As the name implies, interstitial loops are produced by precipitation of a layer of interstitials. A layer of interstitials precipitates initially, which leads to a fault with Burgers vector along 1/3[0001]. If the size of the loop is sufficiently large, transformation in fault and unfault mode would happen depending upon the specific reactions.[17]

In case of sapphire, which the stacking sequence order is like: …Aγ1Bγ2Aγ3Bγ1Aγ2Bγ3Aγ1; a stoichiometric slab of Al_2O_3 is formed by adding two oxygen layers and two aluminum layers in two ways:

…Aγ1Bγ2Aγ3 Bγ1Aγ2/Bγ1Aγ2Bγ3Aγ1…

…Aγ1Bγ2Aγ3/Bγ2Aγ3Bγ1Aγ2Bγ3Aγ1…

The …Aγ1Bγ2Aγ3/Bγ3Aγ1Bγ1Aγ2Bγ3Aγ1…sequence is ruled out as a result of the unfavorable high energy. Only cation sub-lattice is involved in forming the intrinsic fault. If the size of the fault is large enough, unfaulting occurs by the sweep of a Shockley partial 1/3<-1100> across the loop. The reaction is:

1/3<1-100>+1/3[0001] ⟶ 1/3<1-101>

After unfaulting reaction, a mixed type dislocation loop with a perfect rhombohedral Burgers vector finally forms as the cation layers shear to a new position in a sequence order like: …Aγ1Bγ2Aγ3Bγ1Aγ2Bγ3Aγ1…

2. Vacancy loops

Similar to the interstitial loop formation mechanism, high density of vacancies deposited in basal plane triggers the two neighboring atom layers attracting and inclining to contact with each other. In order to avoid this high energy, the unstable condition changes in the following two ways. [18]

In sapphire, vacancy loop with Burgers vector 1/3[0001] is formed at first by removing two oxygen layers and two aluminum layers in the form of a stoichiometric slab of Al2O3:

…Aγ1Bγ2/Aγ2Bγ3Aγ1…

In the next step, the high energy fault that has formed would be relieved in two ways:

One condition is, a stacking fault sequence…Aγ1Bγ2/Aγ1Bγ2Aγ3Bγ1Aγ2Bγ3Aγ1… forms by a 1/3<1-100> shearing. However, this stacking fault can unfault to new positions subsequently by another shear in the same direction. The final sequence would be: …Aγ1Bγ2Aγ3Bγ1/Aγ2Bγ3Aγ1…

Another condition is, new positions are given by directly unfaulting resulting from a 1/3<-1100> shear. New position sequence would be: …Aγ1Bγ2Aγ3Bγ1/Aγ2...

However, no matter what case it is, the final mixed loop will have a perfect rhombohedral Burgers vector. The reaction is:

1/3<1-100>+1/3[0001] ⟶ 1/3<1-101>

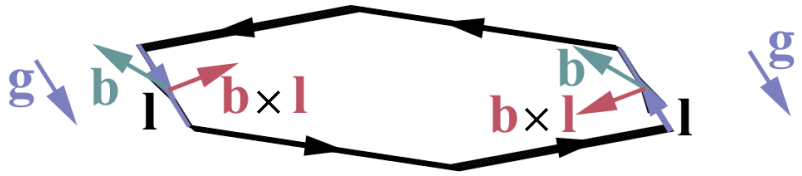

Figure 3.11. 1/3<10-11> dislocation loop showing the position where conditions for contrast invisibility is satisfied for a given diffraction vector.

So far, in sapphire materials, all the dislocation loops found in my experiments are the 1/3<10-11> type. [17,18]

3.4 Etch pits method to reveal individual dislocations

KOH etching of c-plane sapphire wafers

C-plane sapphire wafers etched by the procedure explained in section 2.3 were compared with corresponding transmission topographs. This showed the etch pits correspond to dislocations on the topographs. It was also observed that the morphologies of etch pits appears to be well-defined triangle shape, which are symmetrical and crystallographically oriented (Fig 3.12).

It is not difficult to deduce from the observations made that the etch pits shape occurs due to the differences in reaction rates while chemical etchant attacks the bonds. The dislocations sites in crystal have weaker bonds, higher energy due to stress, and also more unstable compare to the surrounding area, so the reaction rate of etchants would definitely be greater around those dislocation sites. Also due to hexagonal structure of sapphire crystal, the weaker bonds such as the same oxygen ions would be easier to break, which finally create those particular etch pits pattern.

The formation process of boundaries by the accumulation of single dislocations is represented more clearly using the chemical etching technique, which shows in Fig. 3.12(c) and (d).

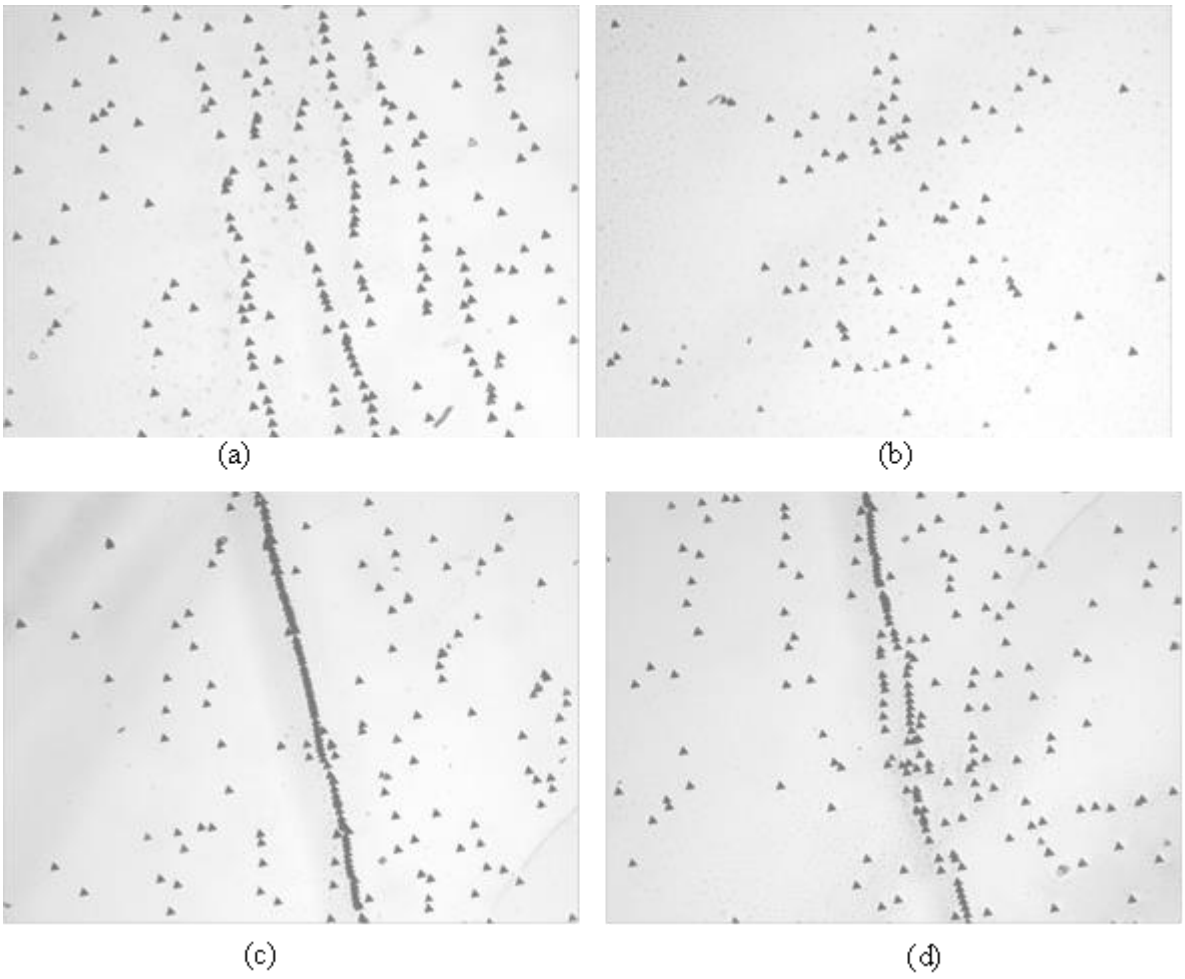

Figure 3.12. Microscopic images of etch pits pattern located in different areas of c-plane wafer. (a) and (b) are the randomly located etch pits pattern, of which the dislocation density are $6.03x10^3$ and $2.59x10^3$ respectively. (c) and (d) clearly illustrate the boundary is formed by accumulating single dislocations which are revealed by etching. The misorientation angles calculated in these two cases are 0.426arcsec and 0.408arcsec respectively.

KOH etching of m-plane sapphire samples

A m- plane wafer cut parallel to the growth direction was first imaged in the transmission geometry to record the 11-20 transmission topography. This topography served as control for comparison with etching. The m-plane wafer was subsequently etching using the procedure detailed in section 2.3. Optical image was taken and locally enlarged using the optical microscope, which is shown in Fig. 3.13 From observation, morphology of etch pits range differently from circular to irregular elliptic shape which elongated in [11-20] direction.

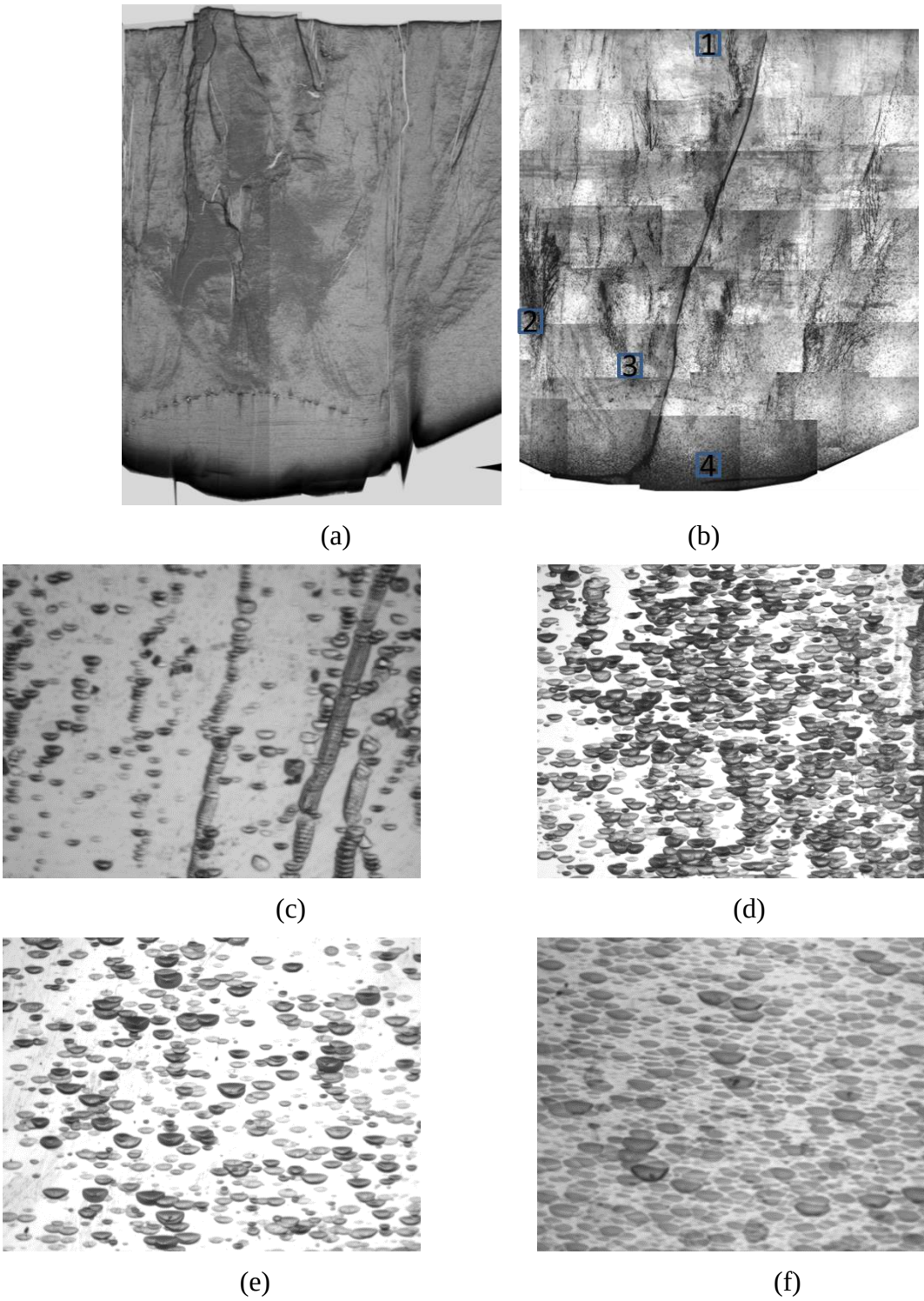

Figure 3.13. (a) Transmission X-ray topograph (g =11-20) of a m-plane wafer and corresponding optical micrograph of etched wafer. Optical micrographs of etch pits patterns in different areas of the m-plane sapphire axial slice.

Comparing the topography and optical images in Fig.3.13, a strict one-to-one correlation between etch pits and dislocations observed in c-plane etched wafer might not be established in

the m-plane etched wafer. These are revealed in the high magnification micrographs in Figs.3.14(a)-(f). On the one hand, some individual dislocations or low angle grain boundaries observed on topographs do not show in corresponding etch pits pattern. All the dislocations present in the region of grain boundaries get etched. On the other hand, where there are no dislocations observed on topographs, several etch pits are observed in the optical micrographs.

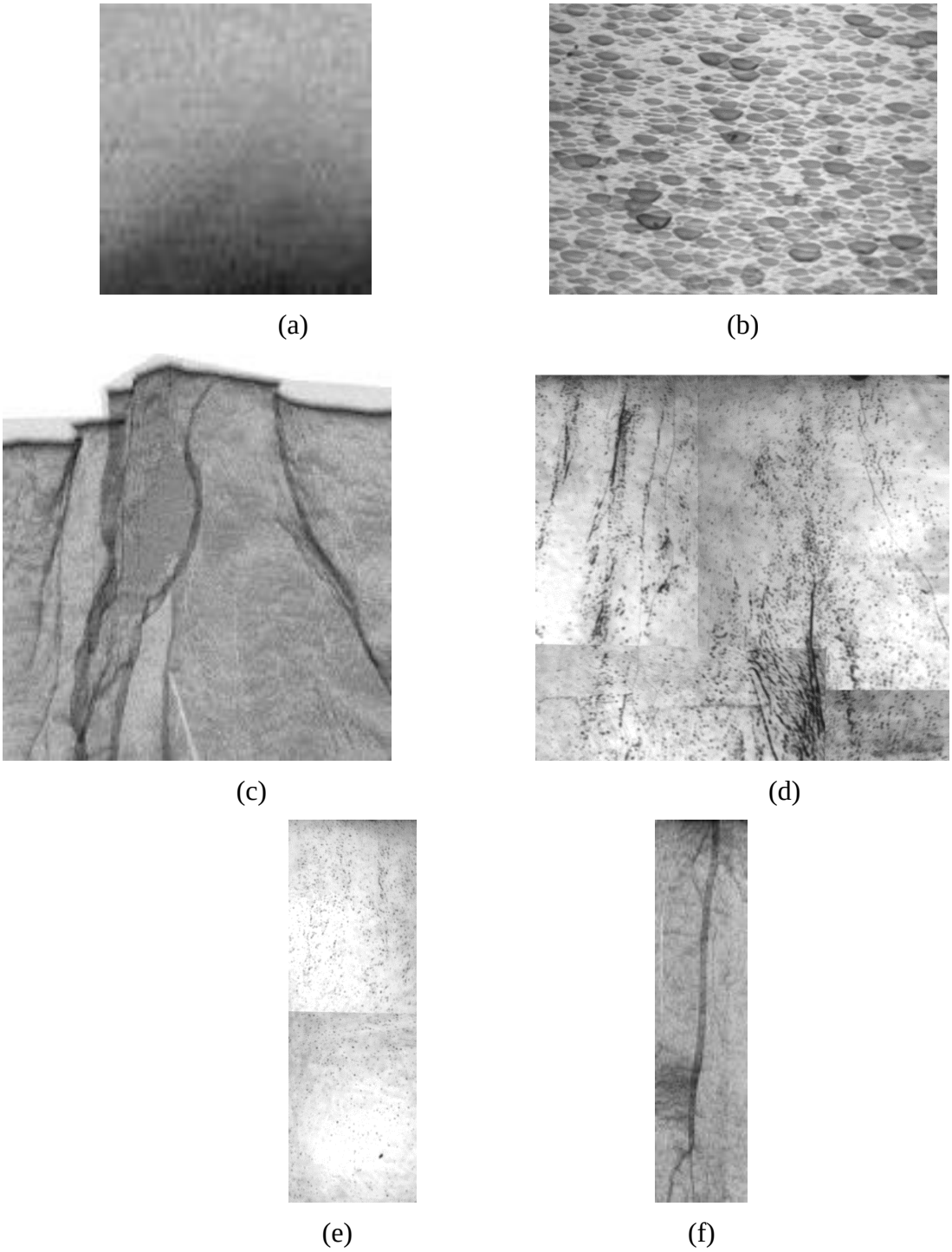

Figure 3.14. X-ray topographs (a), (c), (e) and corresponding optical micrographs showing etch pit patterns (b), (d), (f) revealing the absence of one-to-one correlation between topographs and etch pit patterns for m-plane samples.

To conclude, it is clearly noticeable the shape of etch pits is strongly dependent on surface orientation i.e. on c-plane it is triangular while in m-plane circular. Also the etching reaction rates are different, which leads to much longer time for m-plane wafer to bath in the same molten etchant. This clearly implies the dislocation sites are more unstable and have higher energy level on the c-plane intersection compared to the m-plane. As a result, on m-plane, the dislocation is not sensitive to the etchant which might even not have priority than some underlying surface damage or internal stress in material that probably forms the pit that does not show as a dislocation contrast on topographs.

From the observation of etch pits pattern, the rows of dense etch pits aligned to produce boundaries could be clearly noticed. As these defects play an important role, further experimental analysis is required in the next step for understanding the formation and properties of boundary.[19-22]

3.5 Boundaries and faceting process

Grain boundary is a planar defect existing as an interface separating two different crystallographic orientations. The most commonly observed boundary in our experiments is low angle type. The formation mechanism is shown in Fig.3.15, random dislocations located in a group of parallel slip planes, after a small bend in those planes, dislocations climb and glide to form a vertical plane which have comparably lower energy and symmetrically separate the crystal. Then a tilt grain boundary is formed which consist of a vertical array of dislocations.

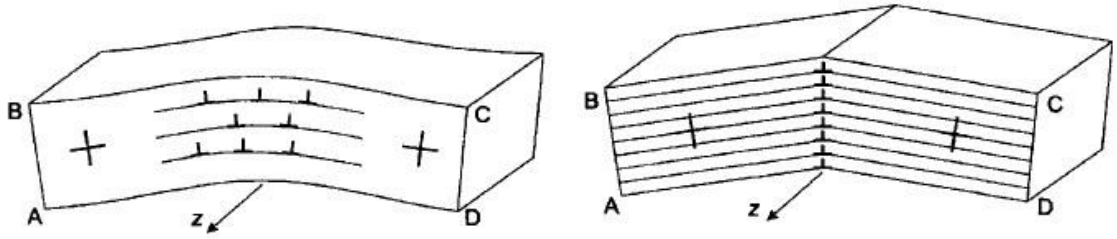

(a) (b)

Figure 3.15. Formation of a low-angle boundary. The orientation of the slip planes is denoted by a cross, (a) Bent crystal with random dislocations, (b) Rearrangement of dislocations to form symmetrical tilt boundary. Both climb and glide are required to produce this boundary.[23]

The low angle here represents the misorientation between two symmetrical parts is equal to the Burgers vector divided by spacing between dislocations (**b**/D~θ) when it's very small.. Therefore, the low angle boundary forming process should be possible to capture as some distinct dislocations in topographs. As a matter of fact, the experimental results shown below confirmed this point of view. [23]

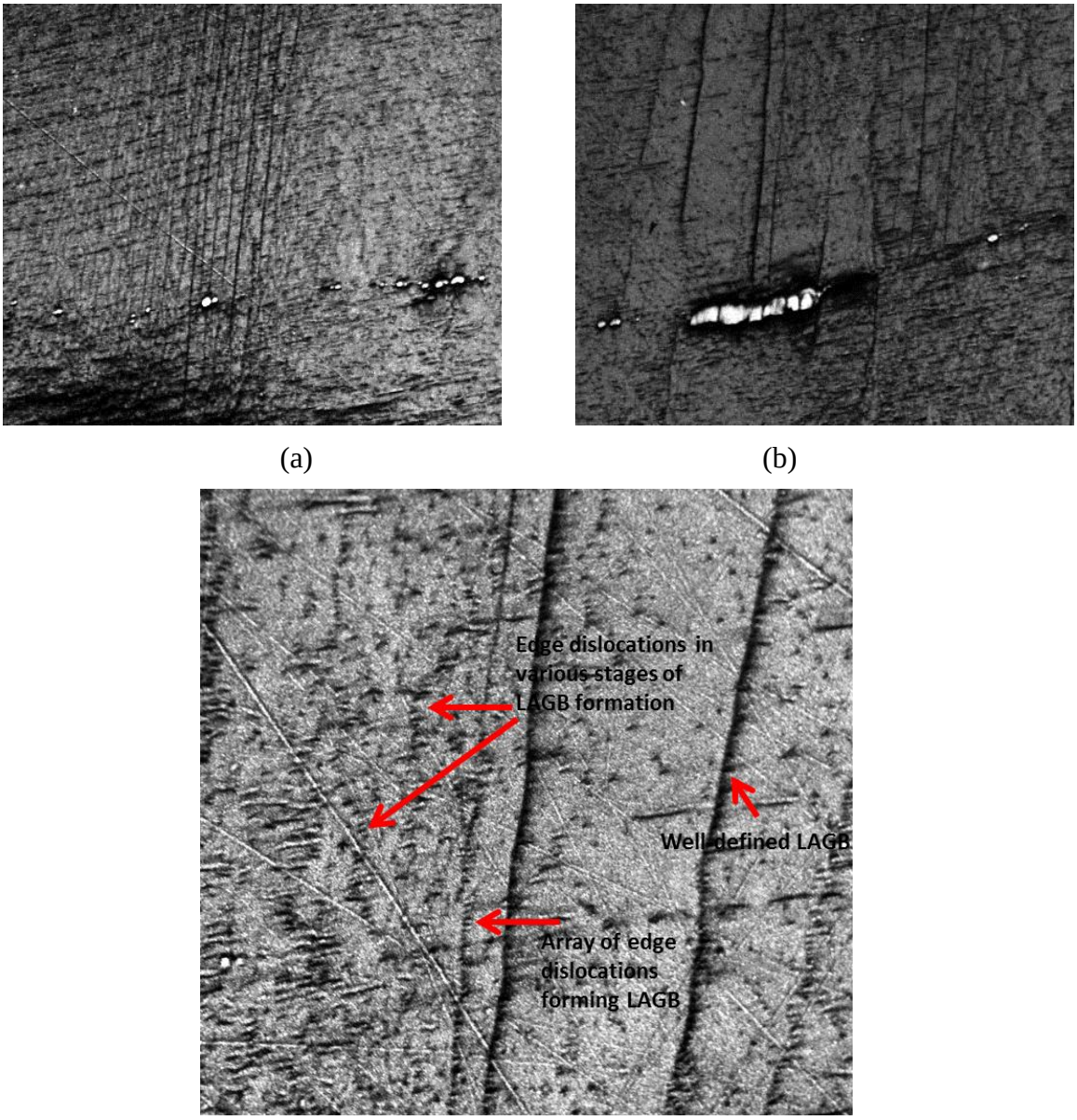

Figure 3.16. High magnification X-ray topography image recorded from m-plane axial slice; showing low angle grain boundaries. (a) Propagating from seed (b) Generated from inclusions; (c) Boundary formation process.

X-ray topographs (Fig. 3.16) recorded from a m-plane slice, shows some low angle grain boundaries propagating from seed (Fig. 3.16(a) and originating from inclusions (Fig. 3.16(b). Details of low angle grain boundaries which is composed of arrays of edge dislocations as well as edge dislocations in process of boundary formation are clearly seen in Fig. 3.16(c). Care should be taken here, as the boundaries can show different contrast on the topograph; both white and black contrast are possible depending on the direction of misorientation across the boundaries. The schematic interpretation of those differences is shown in Fig.3.17.

(b)

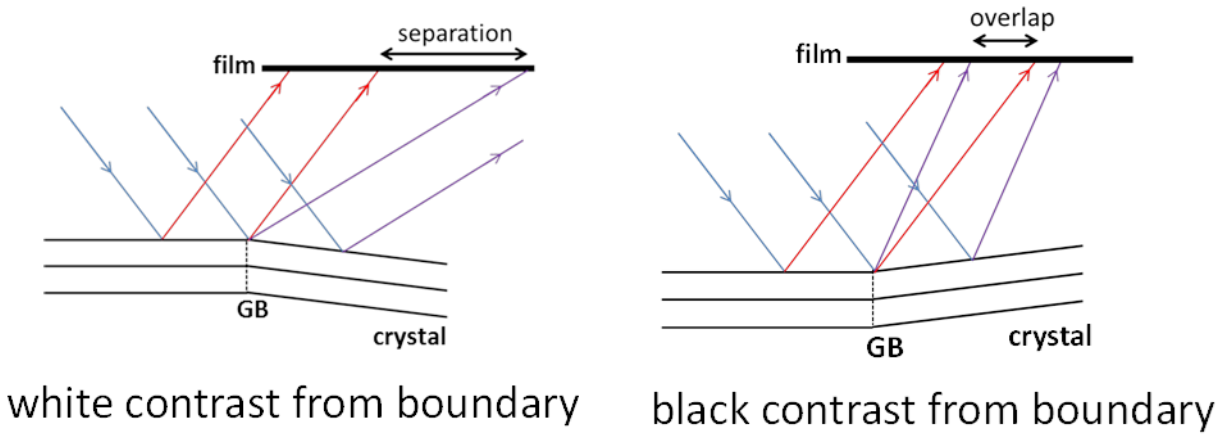

Figure 3.17. Schematic of different orientation contrast mechanisms in creating white and black contrasts from low angle grain boundary.

Difference here is the result of whether the diffracted X-ray beams are converging or diverging, based upon the relative angle between two crystal parts. Overlapping of beams produces black contrast, while separation produces white contrast.

In addition to the grain boundaries in axial slice samples, the boundaries shape in c-plane is quite typical for sapphire grown using melt growth technique. A concentric hexagonal shaped network of low angle grain boundaries in the center is shown in topograph (Fig.3.18) recorded in transmission mode a typical 6-inch c-plane wafer.

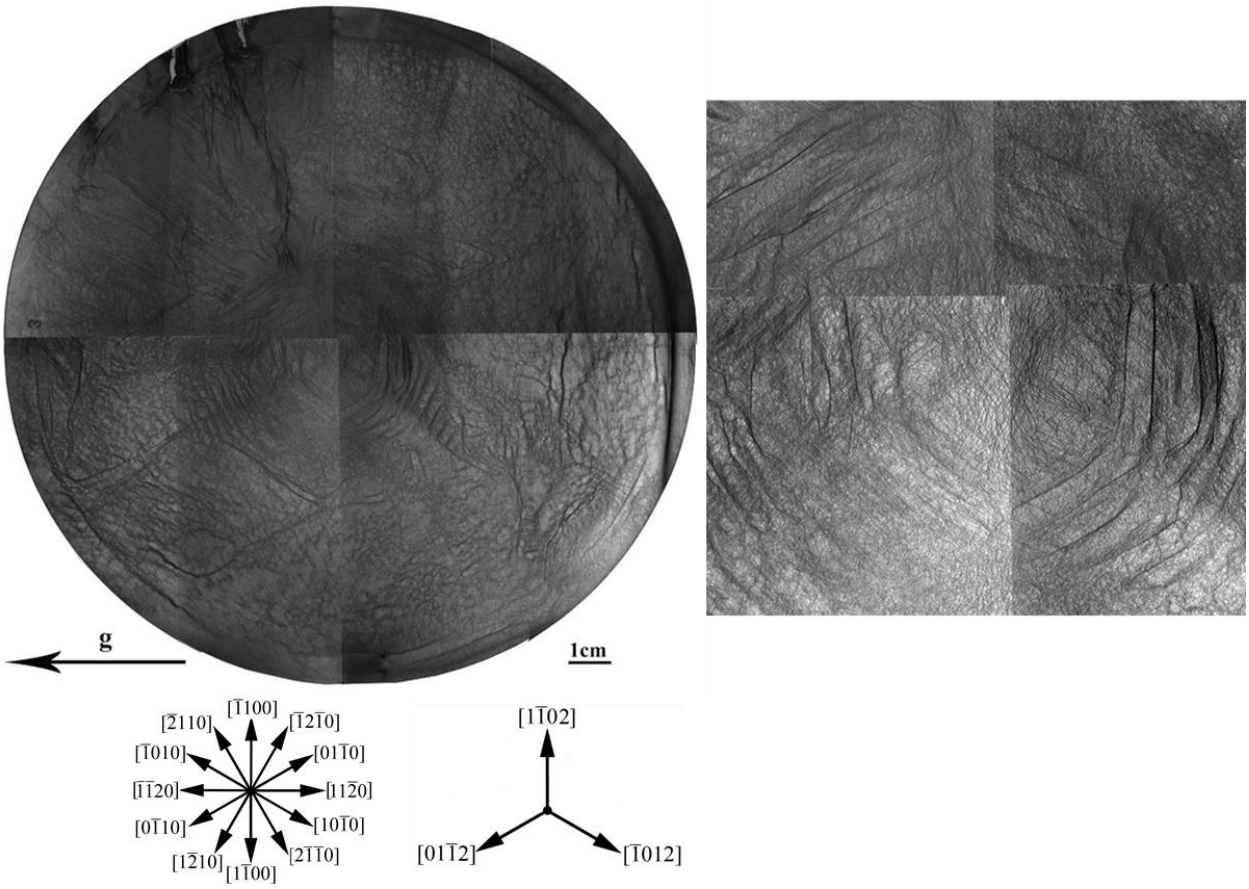

Figure 3.18. X-ray topograph image of a c-plane sapphire wafer and its enlarged central area with concentric hexagonal shaped network of low angle grain boundaries

In this case, crystal faceting is likely responsible for this microstructure. Sapphire crystal can form facets due to the different surface energies of different crystallographic planes. Rhombohedral structure sapphire crystal normally has facets plane as shown below. (Fig.3.19 (a), (b)) [25]

During melt crystal growth, in addition to the c-plane orientation the flat to convex solid-liquid interface can sample low energy r-plane or n-plane orientations which are 57.6° and 61° from c-plane, respectively. Under those circumstances, facets are formed and further growth takes place along these facets resulting in growth sectors separated by growth sector boundaries. Any change in lattice parameter across these boundaries can be accommodated by formation of misfit dislocations. Further, BPDs nucleated from the edges can propagate and accumulate at this growth sector boundary. These dislocations can align to form low energy low angle grain boundaries that we observe lying perpendicular to the <11-20> directions on the c-plane wafer. Figure 3.20 shows the situation for faceting only along c and n-planes. Because the hexagonal boundaries are aligning perpendicular to the a-direction (<11-20>) obviously, which matches well with the intersecting trace between c and n plane. The spoke like trace along <1-100> direction radiating from the center also matches well with the n- plane intersecting trace. It is not hard to infer that the fringes around the central hexagonal boundary pattern might be originated from the different faceting rate in c-plane and n-plane.

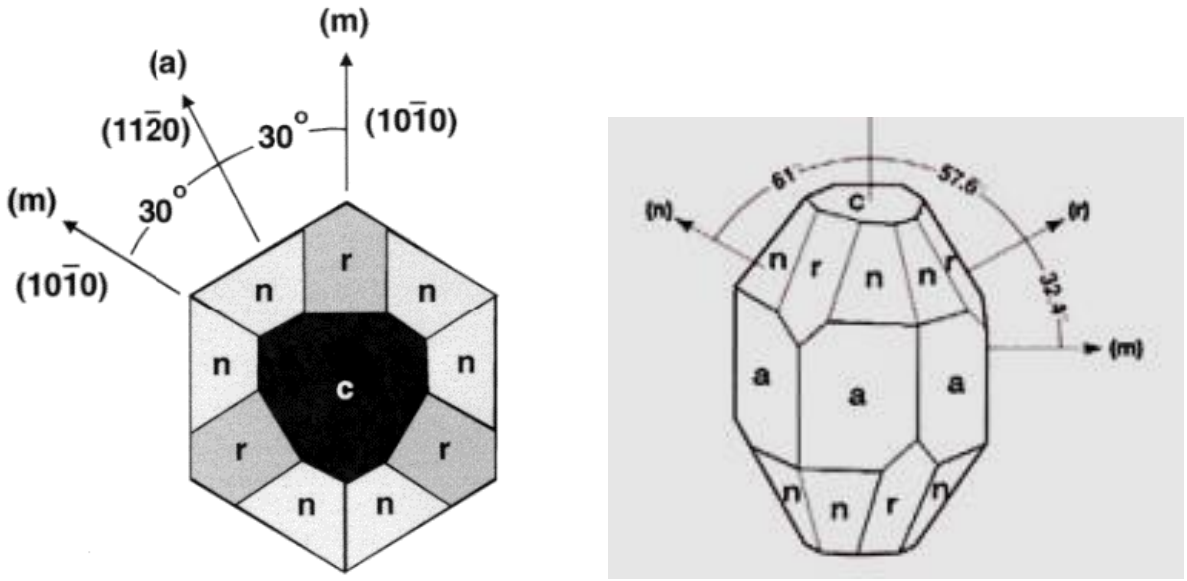

Figure 3.19. Facets in sapphire: **a** – {11-20}; **m** – {1-100}; **r'** – {10-11}; **n** – {11-23}; **n'** – {22-43}; **r** – {01-12}; **c** – (0001)

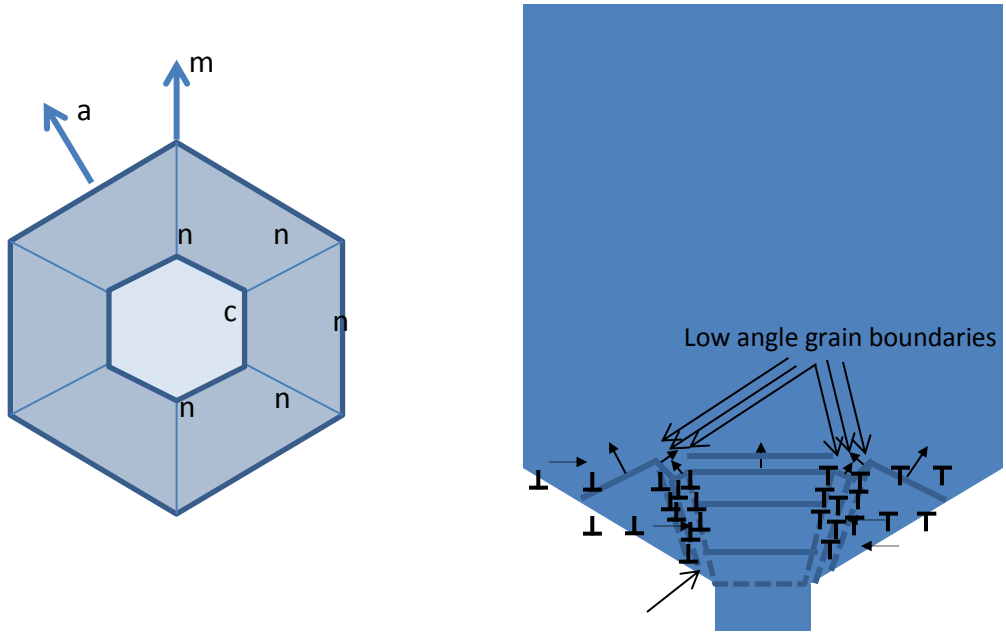

Figure 3.20. n-plane faceting in sapphire single crystal, (a) top view of the faceting surface planes showing the intersection traces of n-n planes and n-c planes, (b) grain boundaries formed by faceting effect and accumulating edge dislocations.

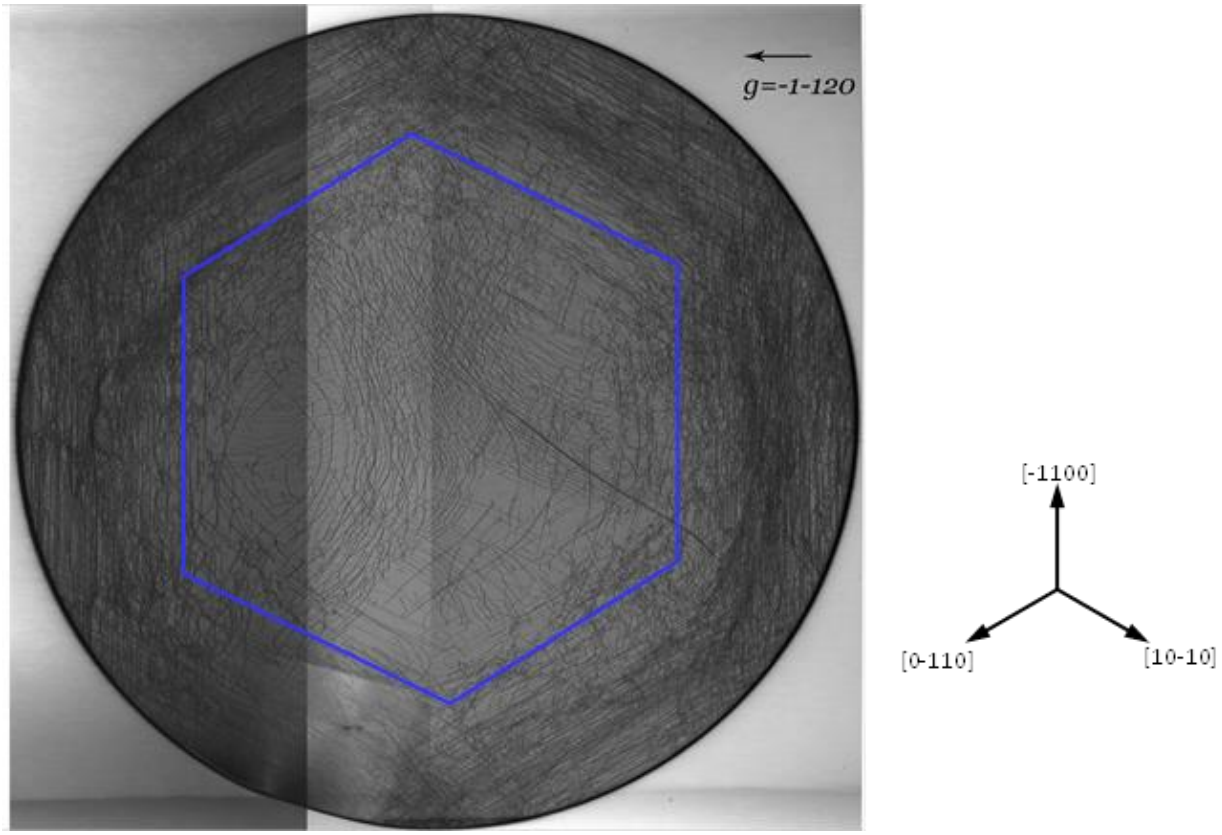

Figure 3.21. Early stages of hexagonal shape boundary formation process by accumulating edge dislocation lines.

In the transmission topograph of a sapphire wafer shown in Fig.3.22, pure edge dislocations were determined to be the dominant type around periphery. Trend is shown that hexagonal shape boundary is about to form by further accumulation of these edge dislocations aligning along <1-100> directions.

Chapter 4. **Defects in bulk sapphire crystal**

4.1 Twinning

Twinning is a phenomenon in which two parts of a crystal lattice structure form mirror image to each other. The two parts, i.e. matrix part and twin part, can be transformed from one to another through certain symmetry operations.

Depending on different operating methods, mainly two types of twinning could be categorized. For type one, twin part can rotate 180° about an axis to have the same lattice orientation as matrix part (rotation twin); for type two, twin part can change to matrix part only by reflecting across a plane (mirror twin).

Twins can be formed either during growth (growth twins) or due to deformation under certain stress conditions (deformation twins).

Annealing twins, mostly found in FCC materials, are rotation twins. In comparison, deformation twins are mostly found in HCP materials such as sapphire , and the relationship between matrix and twin is a mirror reflection across a plane.[26,27]

In the crystal structure of sapphire, only two types of twins can form,i.e. basal twin and rhombohedral twin (as shown in Fig. 4.1). [28]

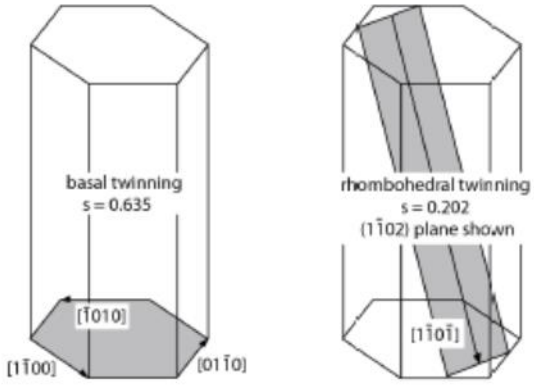

Figure 4.1. Basal twinning and Rhombohedral twinning in sapphire structure

X-ray topography technique can be used to find twin orientation in crystal, since twin structure produces a totally different diffraction pattern from matrix.

Sample selected is a boule (Fig.4.2) which is determined to have twin lamellae confirmed through cross polarizers. Two suspected twin traces intersecting the c-plane on top of the boule are marked in red and blue dash lines. The large angle between the suspected twin plane and the c-plane on top indicates those are most likely rhombohedral twins whose shearing plane is r-plane ((1-102)).

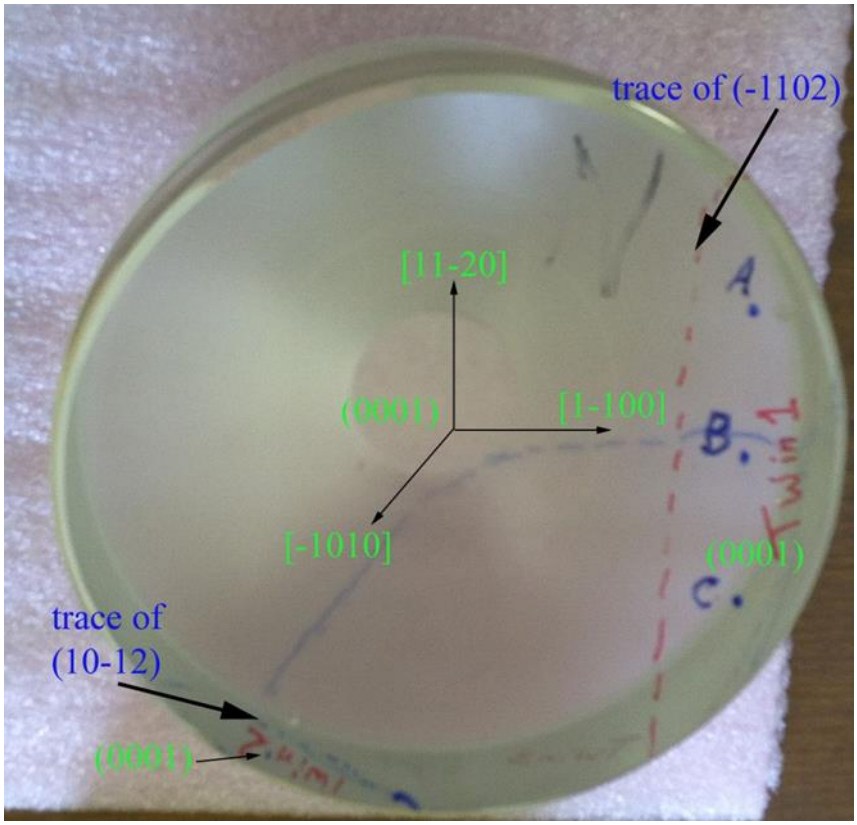

Figure 4.2. Sapphire boule containning twin lamellae

The rhombohedral twin of sapphire is caused by a compression stress loading along c-axis. A shearing stress is applied on the twinning plane (-1012) reorients the crystal lattice which finally creates a 115.2° angle between the c-plane (0001) in the twin part and in the matrix crystal. (Fig. 4.3)

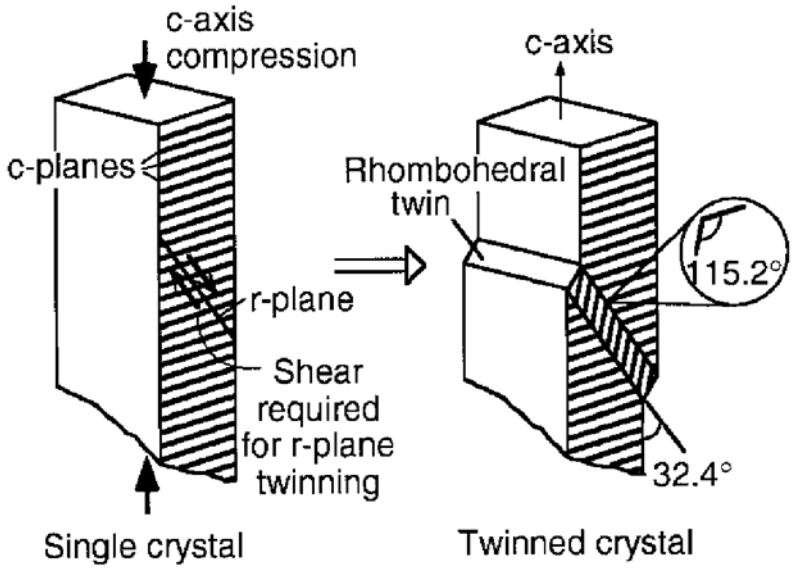

Figure 4.3. Sapphire rhombohedral twinning mechanism

For further understanding the crystallographic relationship and visualizing twin lattice in an atomic level, a structure model of rhombohedral twin in sapphire was simulated using Crystal Maker Software. In Fig.4.4 , the twin model is projected, and the basic crystallographic elements are denoted respectively on (11-20) projection in terms of shear plane which serves as the plane of symmetry of the crystal. Deformation twinning is achieved by a homogenous shear stress parallel to the composition plane K_1 which aligned to the shear direction η_1. In this projection view, K_1 plane here can be imagined to be the mirror reflecting matrix to the twin. And the angle calculated between the c-planes of twin and matrix is 115.2°. Then, according to the geometry relationship, the twinning operation is directly rotating the c-plane normal 64.8° about the [11-20] axis clockwise in the view of Fig.4.4.

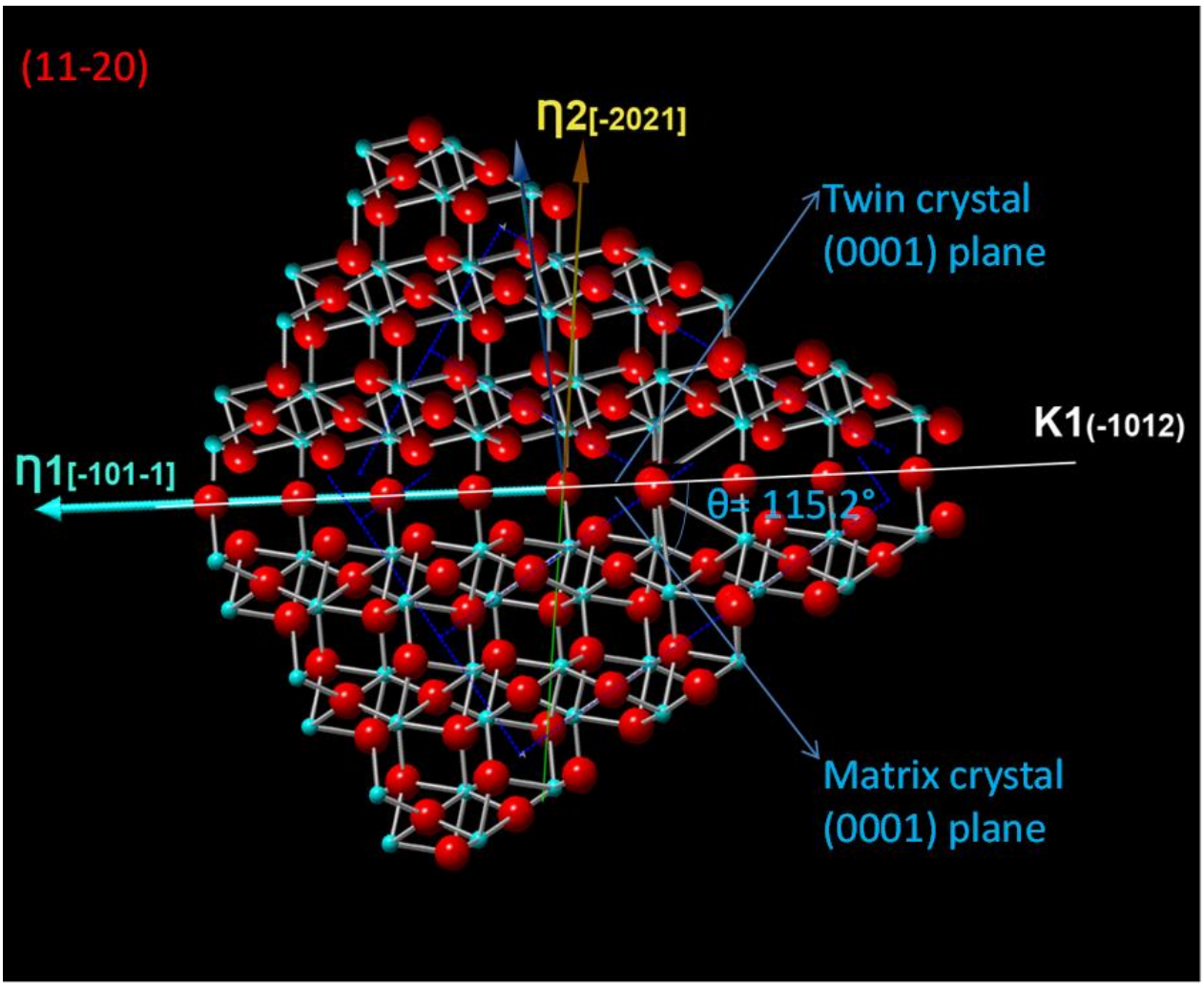

Figure 4.4. Simulation image of rhombohedral twin structure model in sapphire

Therefore, for confirming that the observed twins are rhombohedral twins, back reflection diffraction patterns were recorded from the matrix and twinned regions in the boule shown in Fig. 4.2. Considering the tiny size of twin lamellar, very small beam size (2mmx1mm) should be employed to preventing too much noise in background. X-ray diffraction pattern was recorded for those spot areas in back reflection geometry. The experimental setup is shown in fig.4.6.

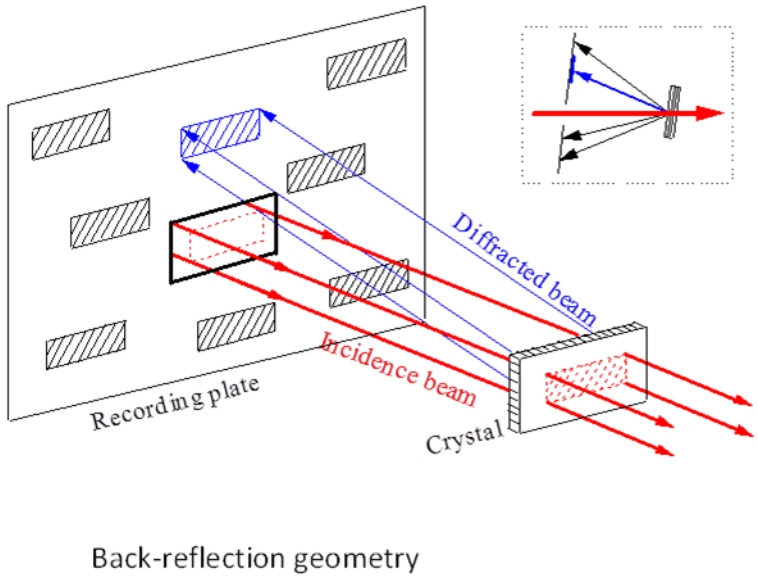

Figure 4.5. Experimental setup in back reflection geometry

A scan of X-ray film recorded from spot #1 in back reflection geometry shows in fig. 4.6 (a). Two patterns are captured in this image, though the twin spots whose thickness in microscopic level are hard to identify without further enlarging. The blow up twin spot shows in fig. 4.7 (c), and the independent twin pattern is marked and filled out from the overall topograph (fig. 4.7 (a)). The orientation of matrix crystal is figured out with the help of simulating by Laue Program (fig.4.7 (b)), which the top direction is [1-210] with the [0001] direction surface normal.

Regarding the operation method to reflect matrix to rhombohedral twin geometry orientation discussed above, same operation mode can be utilized to get the twin back reflection pattern from matrix one. The Fig. 4.8 (b) is the pattern simulated after 64.5˚ rotation about Y axis, which equals to <11-20> direction in crystal coordinates system, from matrix back reflection pattern, Fig. 4.6(b). Comparing the twin pattern recorded from experiment (fig.4.8 (a)) with the simulated one, they match very well to each other, which confirms the identity of rhombohedral twin of twin type.

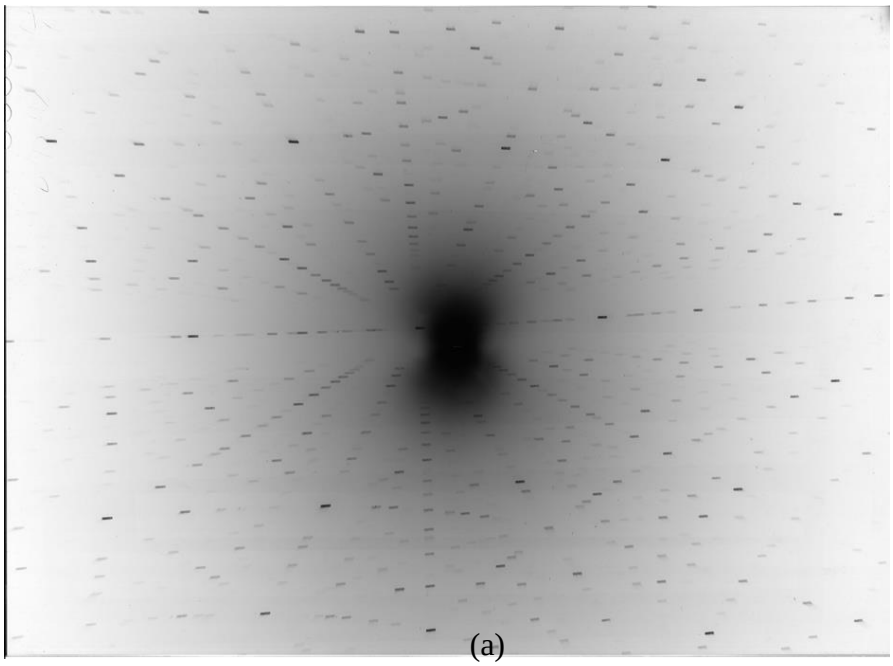

(a)

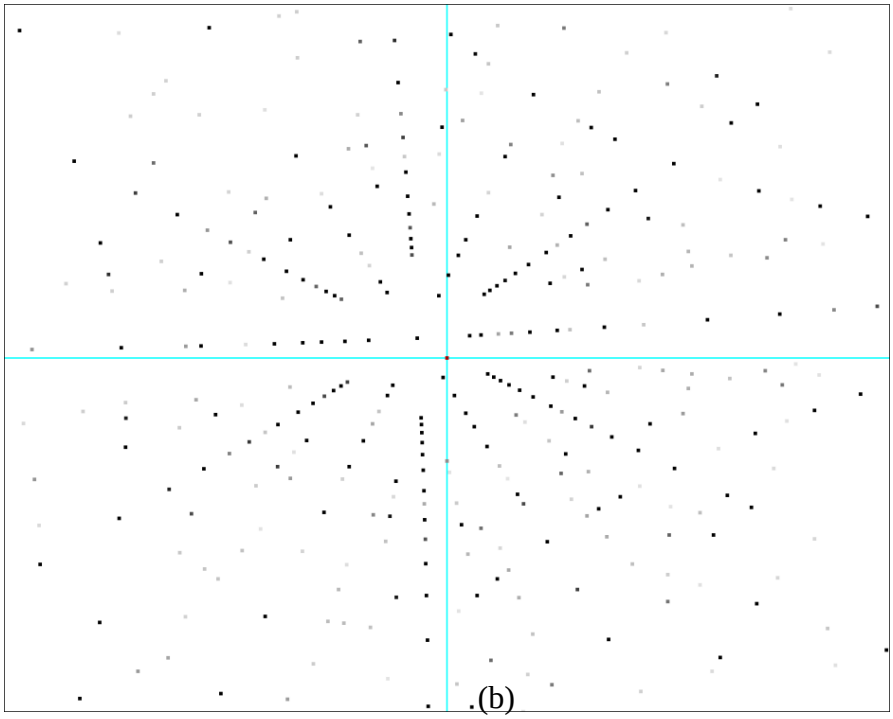

(b)

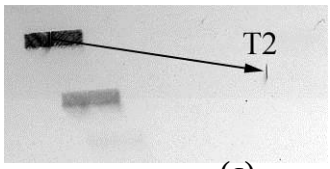

(c)

Figure 4.6. (a) back reflection pattern recorded from matrix and twin, however the twin layer is too thin to discern; (b) simulated (0001) back reflection pattern from matrix; (c) enlarged diffracted twin spot.

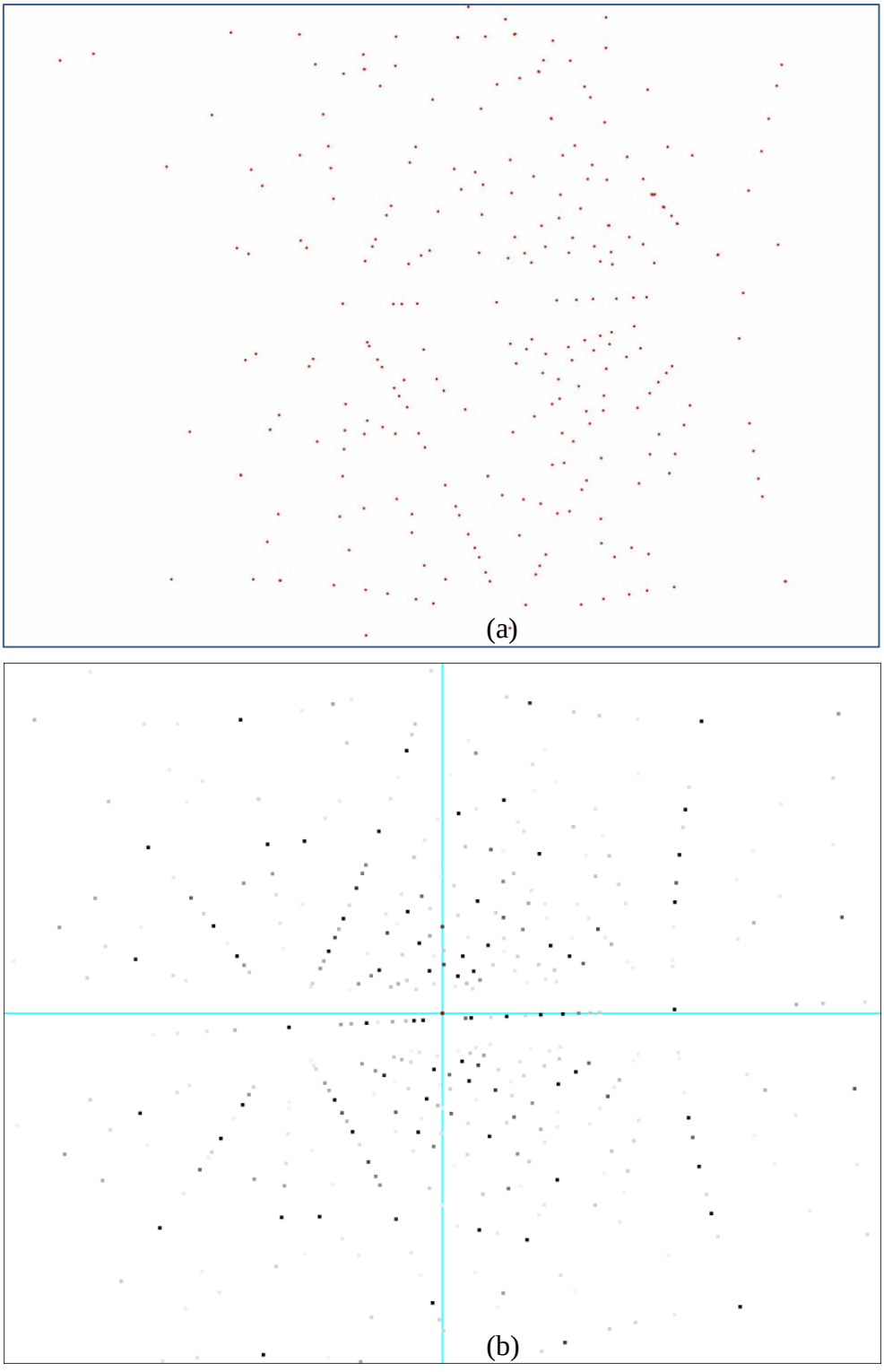

Figure 4.7. (a) Back reflection pattern of twin lamellar from the X-ray film in Fig. 4.6(a); (b) simulated back reflection pattern of rhombohedral twin orientation corresponds to (10-12) orientation.

4.2 Cracks and Stress mapping

SMART technique

Stress incurred results in different thermal treatments or specific growth circumstances during various stages based upon particular crystal growth technique plays a crucial role for generating several defects and promoting their propagation in crystal, which not even produce failure but also directly affect the multiple properties and performances of crystal devices. Due to the technological importance in understanding the origin of stress and figuring out the relation between stress and various defects requires immediate attention.

For this purpose, synchrotron white beam topography combined with synchrotron white beam reticulography technique was employed as a stress detecting method that was developed in our lab. In addition to being a nondestructive characterization technique, no damage would be induced for measuring the deviation of orientation from local lattice plane through ray tracing by topography imaging, which is known as stress mapping analysis via ray tracing (SMART) technique.

The fundamental concept of this technique is stress can cause lattice plane orientation change, which can be described by plane normal vector. The relationship could definitely be established between the deviation of lattice plane and internal stress. The plane normal change as a result of stress loading is illustrated in Fig.4.8. When tensile stress loads in y direction, stress free plane normal $\mathbf{n}_0$ would change to $\mathbf{n}$.

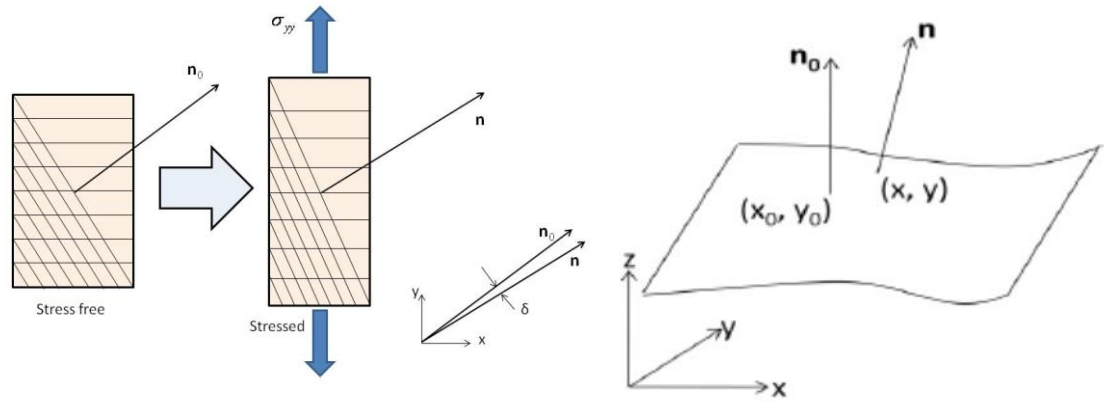

(a) (b)

Figure 4.8. (a) Illustration of change in lattice plane orientation due to the loading stress; (b) A schematic of a distorted crystallographic plane. n is the plane normal vector

In Fig. 4.8(b), $\mathbf{n}_0$ (x, y, z) is the plane normal vector at a strain free location and $\mathbf{n}$ (x, y, z) is the plane normal vector at any general (strained) location (x, y, z). In the whole crystal area, (fig.4.9) the strained plane normal $\mathbf{n}$ in (x,y,z) satisfies the equation below with the strain free plane normal $\mathbf{n}_0(x_0,y_0,z_0)$:

$$\mathbf{n}(x,y,z)= \mathbf{n}_0-\nabla[\mathbf{n}_0.\mathbf{u}(x,y,z)]$$

Specific plane normal in certain point of whole area could not be hard to figure out using data on the recording film and the geometry of setting when doing experiments. **u**(x,y,z) in the equation above, representing plane displacement illustrated in fig.4.10 , satisfies a relationship with Ɛij:

$$\varepsilon_{ij}=1/2\left(\frac{\partial ui}{\partial j}+\frac{\partial uj}{\partial i}\right)$$

Finally, σ_{ij} could be calculated using ε_{ij}:

$$\sigma_{ij}=C_{ijkl}\varepsilon_{kl},$$

Where the C_{ijkl} is the material stiffness matrix.

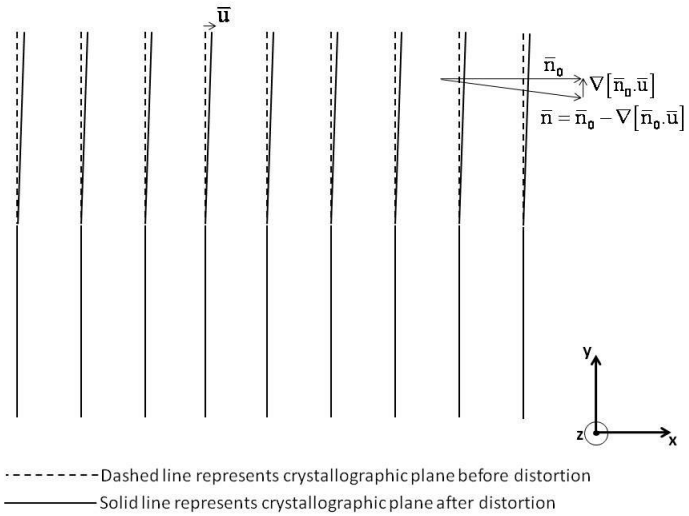

Figure 4.9. Schematic of plane normal variation and its relationship to the divergence of displacement component

Considering the spatial stress σ_{ij} is a tensor including nine components, (Fig. 4.10) in order to calculate, at least nine coordinates of a same point in three independent reflection spots are needed for solving those linear equations separately.

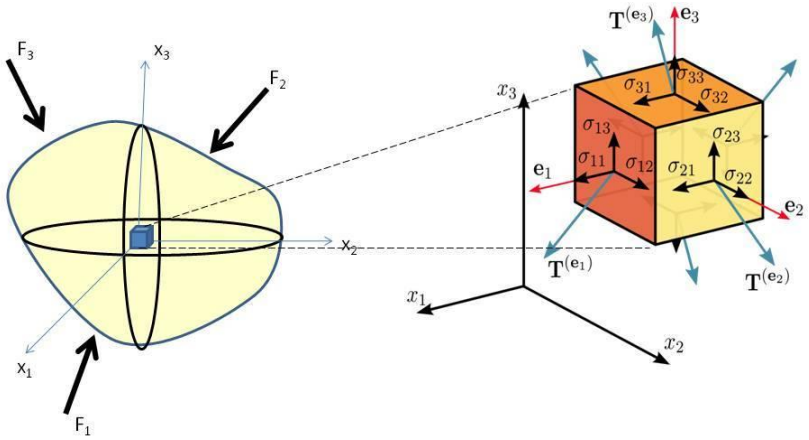

Figure 4.10. Schematic of nine components in stress tensor in a solid object under applied stress

Care should be taken here, that all the three reflection spots selected should have the same penetration depth, (Fig. 4.11).

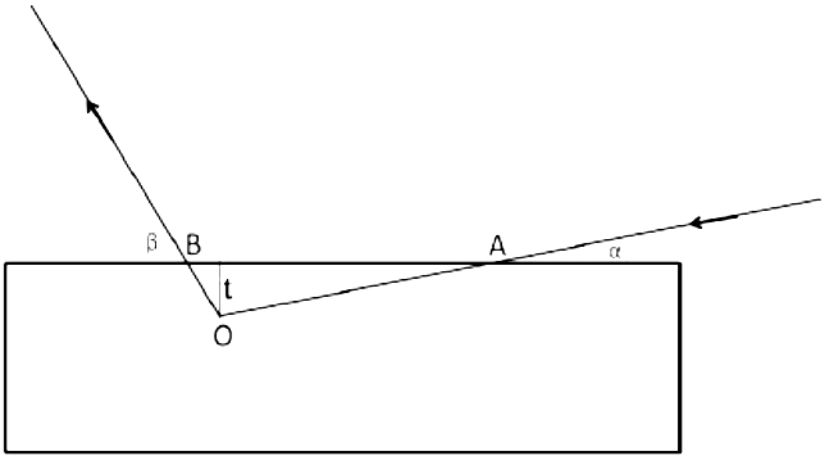

Figure 4.11. Schematic of penetration depth for specific crystal material

The calculation of the penetration depth expression is given by:

$$t_p = \frac{1}{u(\lambda)[cosec(\phi 0) + cosec(\phi h]}$$

ϕ_0 is the angle between the beam and the entrance surface of the crystal,

ϕ_h is the angle between diffracted beam and the exit surface of crystal.

$u(\lambda)$ is the mass absorption coefficient which is the function of wavelength.

Except the inconsistent depths of different reflection spots, another factor induced by penetration depth might results in systematic errors. The stress σ_{ij} we calculated in this step is the average weighted value over a certain depth in crystal due to the exponentially decaying intensity of X-ray. When converting this to the real stress field, there is a bottle neck for figuring out the convolution function described by the real stress contribution weighted by decaying X-ray in depths, because it might not be a simple consequence just involving the dimension of depth.

Moreover, since the X-ray is more sensitive to plane normal, discrepancy exists between the high precision requirement and the limited capability for measuring during experiment, which places an obstacle for quantifying stress locally.

However, qualitative analysis still can be achieved using this method. Lots of experiments have been carried out. The experimental setup is the same illustrated in fig.4.12.

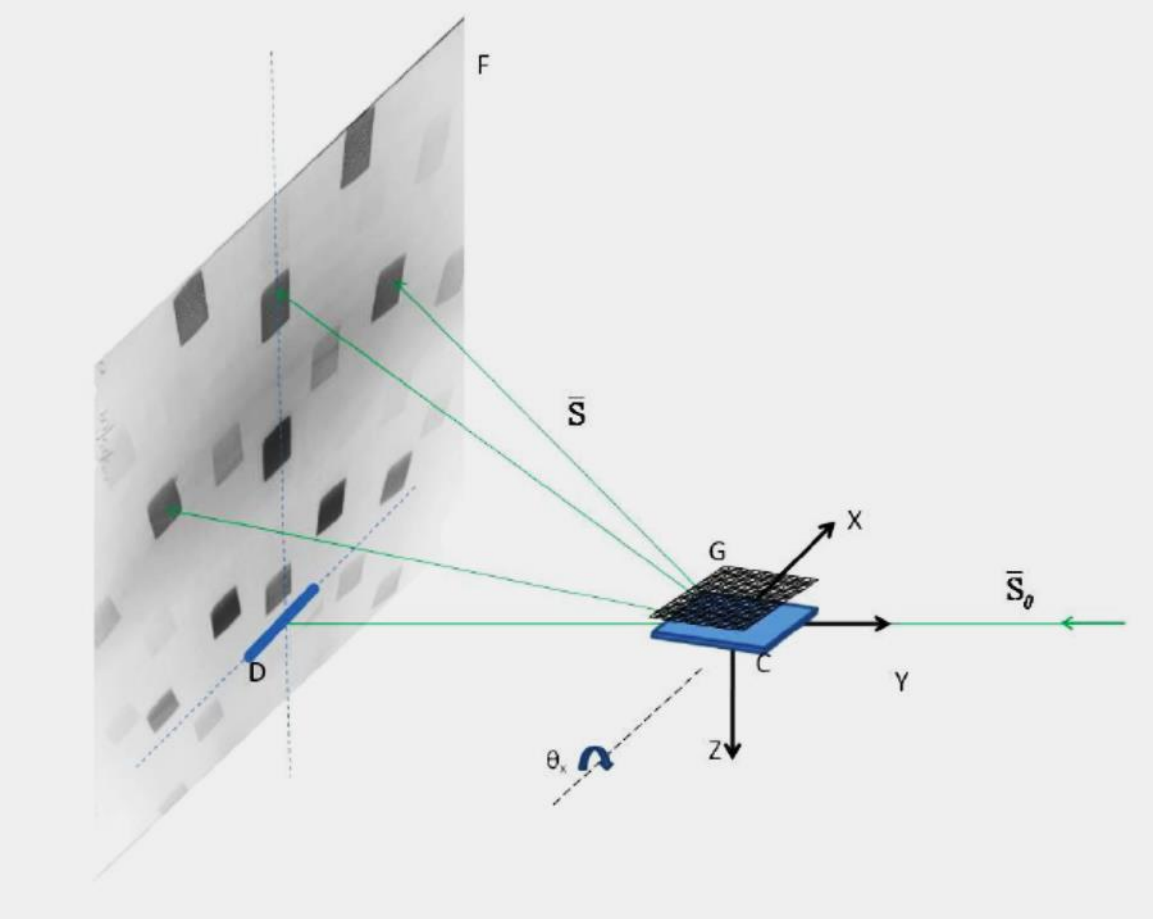

Figure 4.12. Illustration of experimental setup for reticulography in reflection geometry

Due to the large thickness of the bulk samples studied, only the reflection geometry could be successfully employed considering the X-ray intensity absorption. A fine scale tungsten grid which can absorb X-ray placed on top of the sample utilized as a mark of the diffracted beam by producing different contrast. The size of the grid is 400x400μm and the thickness of the grid line is 100μm, which defines the resolution of the stress mapping. Multiple reflection spots are recorded simultaneously on the film. Two important things need to be noted, one is the adjusted beam size and the sample to film distance selected should balance between recording more and clearer reflection spots but as less overlapping as possible. The other is to try to catch the same reflection pattern when horizontal distance between beam and sample changes while exposure takes place for the whole sample, which makes it possible to analyze the whole sample in every recorded reflection indexes.[30]

For qualitative analyzing the stress distribution in crystal, that the shape and the borderlines of grid diffracted locally is a direct reflection of local lattice stress condition. In general, four types of distortion modes in reticulograph implying stress are shown in Fig. 4.13.

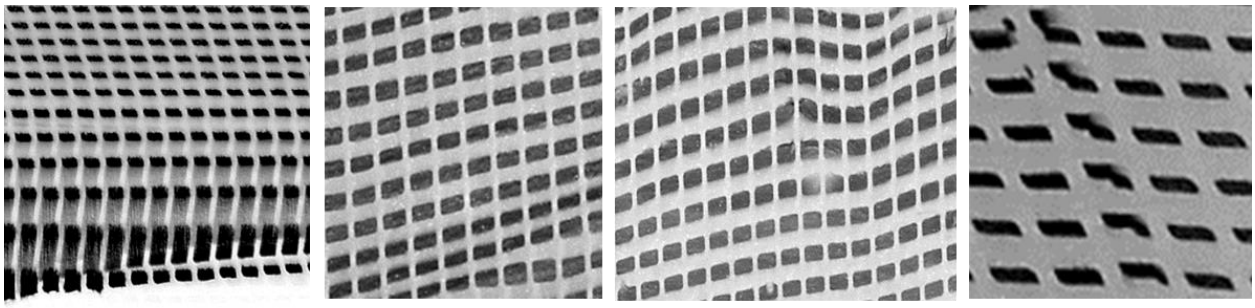

(a) (b) (c) (d)

Figure 4.13. Four types of distortion modes in X-ray reticulograph due to the residual stress

In Fig.4.13 (a), there is a relative expansion of squares in the bottom rows. In Fig.4.13 (b), the lines composed of squares are compressed compared to the well ordered squares above. In Fig.4.13(c), an obvious curve in lines is observed. In Fig.4.13(d), a displacement of grid image is observed.

However, some cases also involving displacement required careful attention and had to be considered seperately. Fig.4.15 (a) is a blow up image of reticulograph full of scratches which only shown in different contrast. This is the normal appearance of scratch as results of bad polishing. But in other cases, certain stress might be incurred by the scratches present which affects the results, surface damage usually is caused after the crystal growth. (Fig.4.14(b)) This should not be taken into account for the stress generated during growth. In Fig.4.14(c), the displacement of crack due to different diffracting orientations should not be misunderstood as residual stress either.

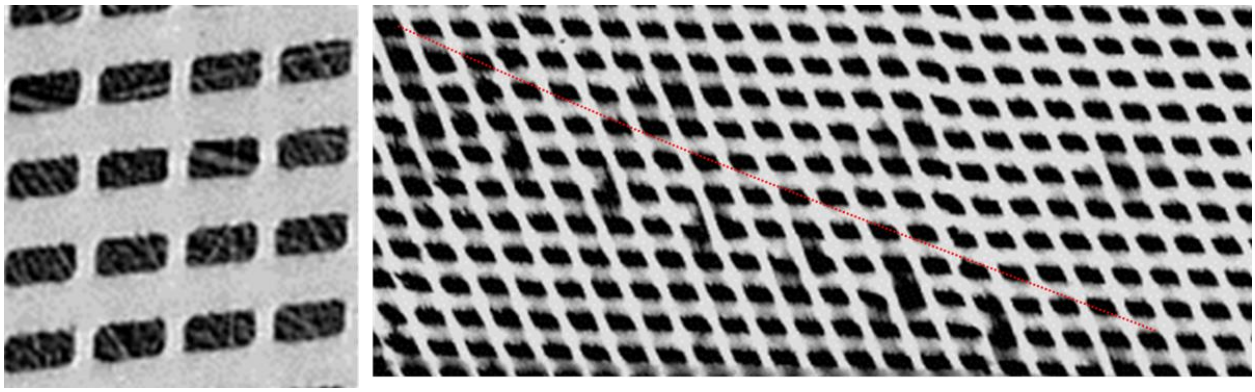

(a) (b)

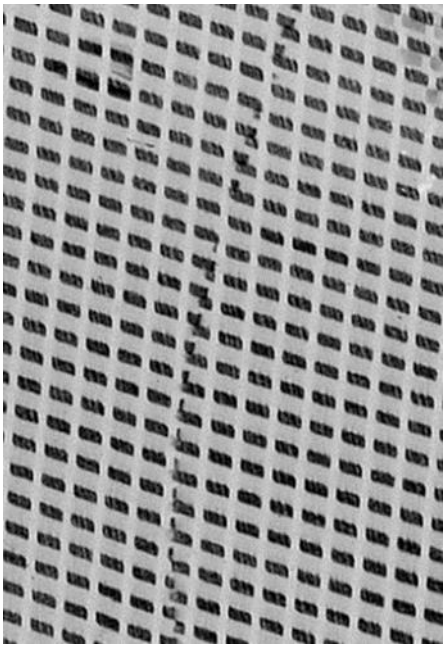

(c)

Figure 4.14. (a) A blow up image of reticulograph full of scratches; (b) distortion caused by surface damage; (c) displacement near crack edges.

Besides that, for rigor, during the analysis, another important thing needed to clear is, on account of the resolution of reticulograph is limited by the scale of the grid, which make stress features smaller than the area of grid invisible; undistorted grid not only means stress free but minor stress. In case of fig. 4.15, no distortion is found in reticulograph according to those dislocation features in topography. It might be that stress is totally relieved by generating dislocation, or still a very tiny residual stress was left but undetectable by qualitative assessment. Nevertheless, stress in this level likely are not responsible for crack nucleation.

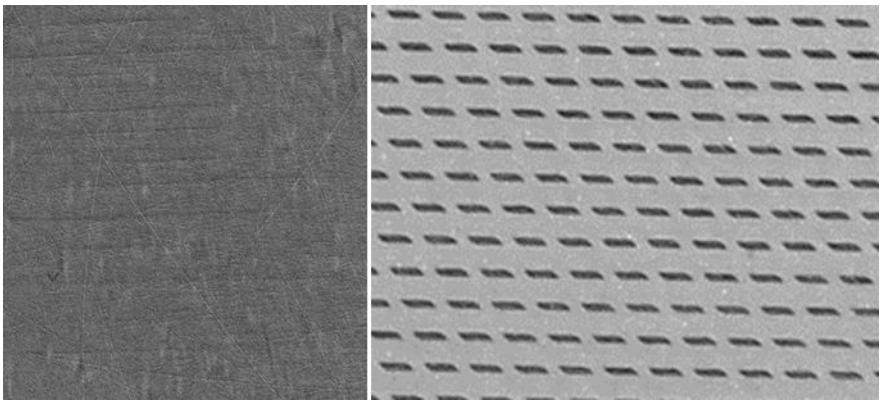

Figure 4.15. X-ray reticulograph image of dislocations

Stress analysis of as-grown samples

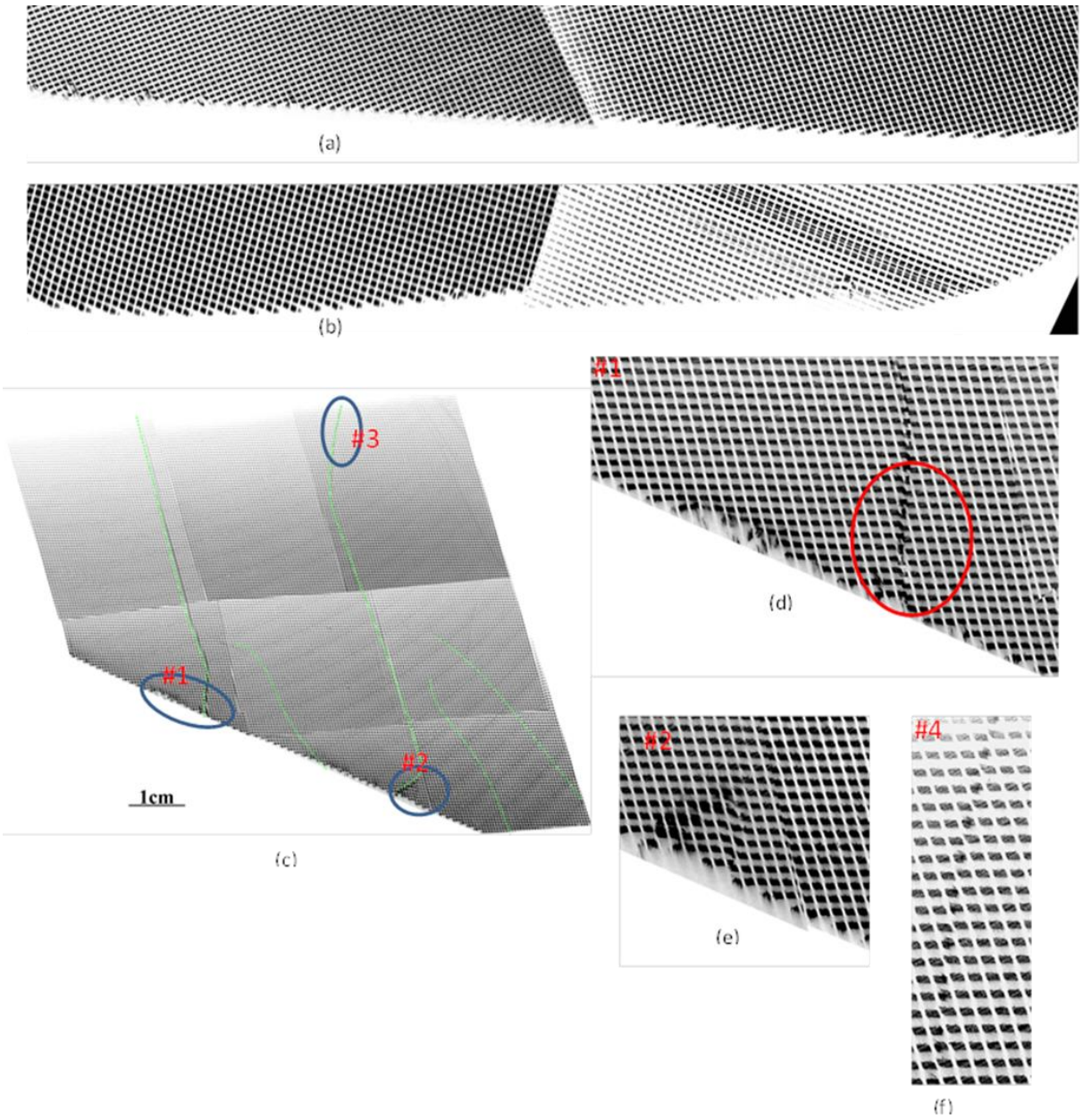

Figure 4.16. Significant residual stress near shoulder regions of the boule

With the help of reticulograph, three typical types of stress visualized due to the growth methods needs further discussing.

a. Stress near shoulder of boule and the surface contacting the wall

Due to the melt growth method that normally utilized for growing sapphire, residual stress always observed around the area contacting the crucible wall, which is usually around shoulder and the vertical area, indicates relative large stress locally distributed during growth. Fig.4.16 (a), (b) is the shoulders region from one of the representative boule samples where relative large distortion located near the edges. Stress concentration in those areas always accompanied with cracks, like Fig.4.16 (c), cracks are marked with green lines. Some local high magnification images where crack ends in shoulder appears to show significant distortion, where the other area along the crack shows much smaller residual stress. (Fig.4.16 (f)) Gathering all the clues discussed above, cracks in this case are possiblly generated by origin stress during growth near shoulders.

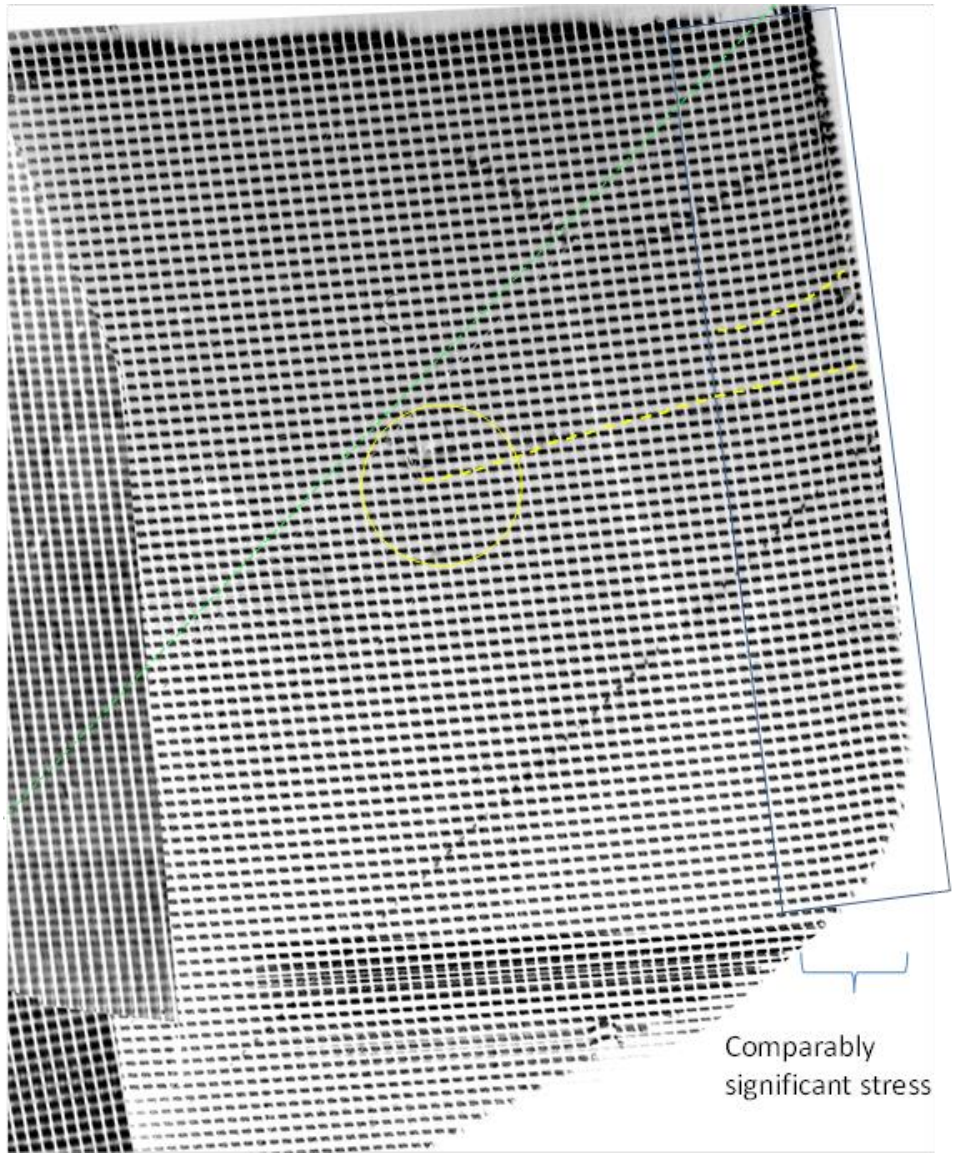

Figure 4.17. Significant residual stress located in boule regions close to the crucible wall

Same case is found near the crystal contacting the wall. Significant distortion in blue squares marked in Fig.4.17 implies the reason for the origins of those cracks, marked with yellow lines, and twin, marked with green lines.

b. Stress near the seed

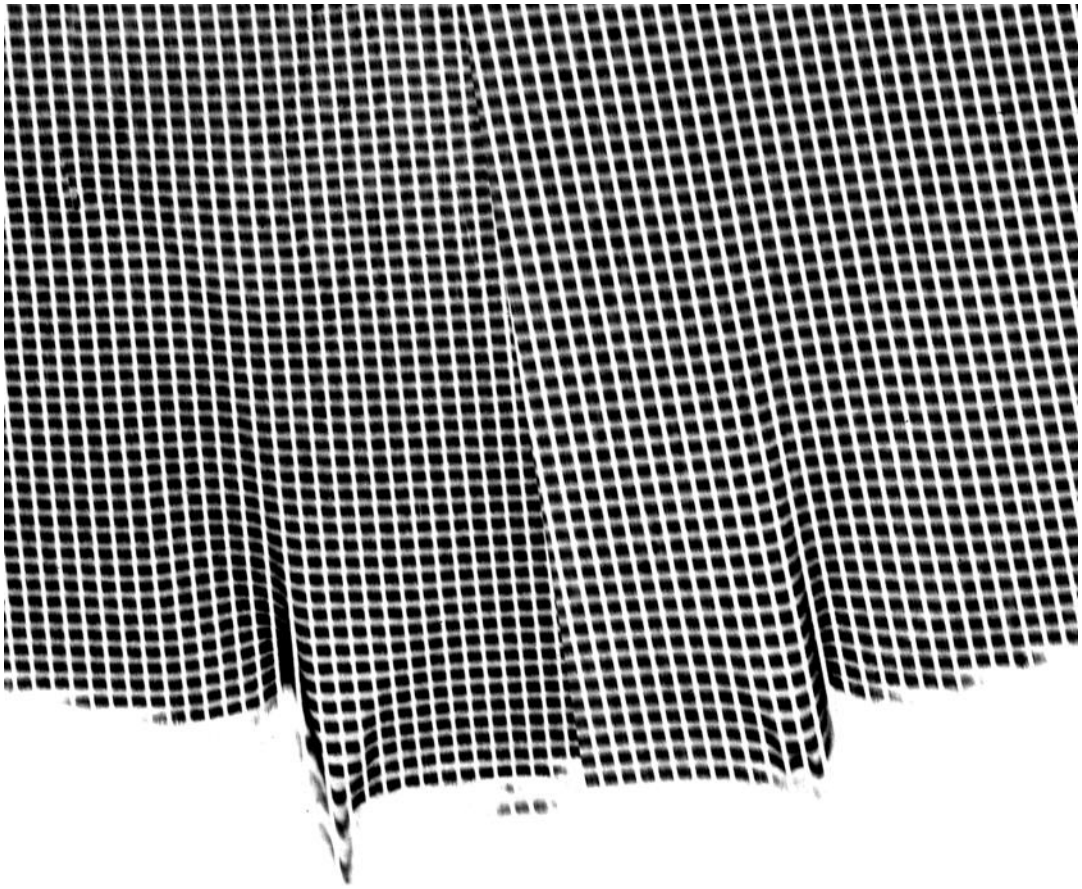

Figure 4.18. Residual stress near seed

Large distortion near the seed edges are normally found in boule, an example is shown in Fig. 4.18. It might be the connecting points between melting seed interface and the melt aluminum oxide. Many defects even large boundary may form and propagating along the vertical direction due to the accumulation of dislocations due to stress originates from this area.

c. Stress near bubbles

There are lots of bubbles always produces in the final stages of growth. Some bubbles can be created in the center region of the boule occasionally also. Certain stress might be induced around those bubble defects. Fig.4.19 shows such images. Stress marked with red circle in the reticulograph corresponds to the optical photo image of those bubble areas.

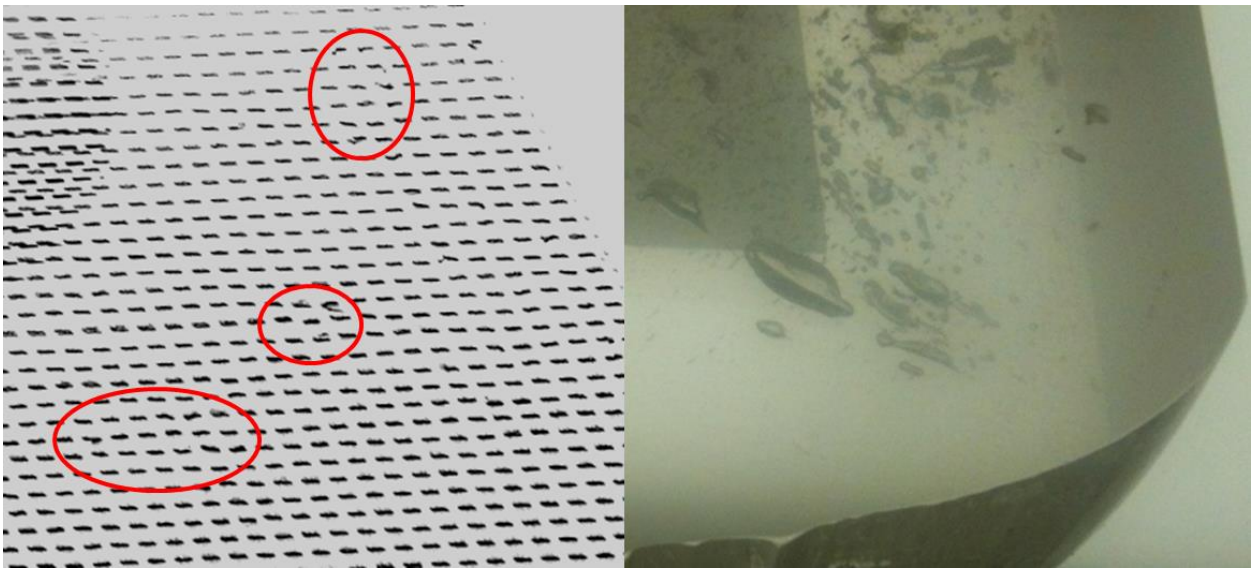

Figure 4.19. Residual stress near bubbles

It should be noticed that only the stress near the bubbles very close to the surface can be detected due to the limited penetration depth.

1. Residual stress analysis of different defects which might trigger cracks due to growth.
   a. Boundary

In general, all the boundaries showing a different contrast in topograph are relevant to certain visible distortion in reticulograph. Some are even very remarkable. An example is shown in Fig.4.20 (a), (b), where the (a) (b) represents the left and right side surfaces of the axial bulk sample cut parallel to the a-plane respectively. Two low angle boundaries involving significant distortion are observed almost at the same height in two side surfaces of the crystal which are highlighted by red lines. Through the extent of distortion, we can tell that similar stress variation along the growth direction in two side surfaces is revealed from the reticulographs. All the stresses are concentrated before but relieved a lot after the significant boundary, while all twin and crack defects are also locating before the boundary, though relieving the increasing stress to some extent. The twin and crack shows as white contrast in the reticulograph which are highlighted by the green dash lines.

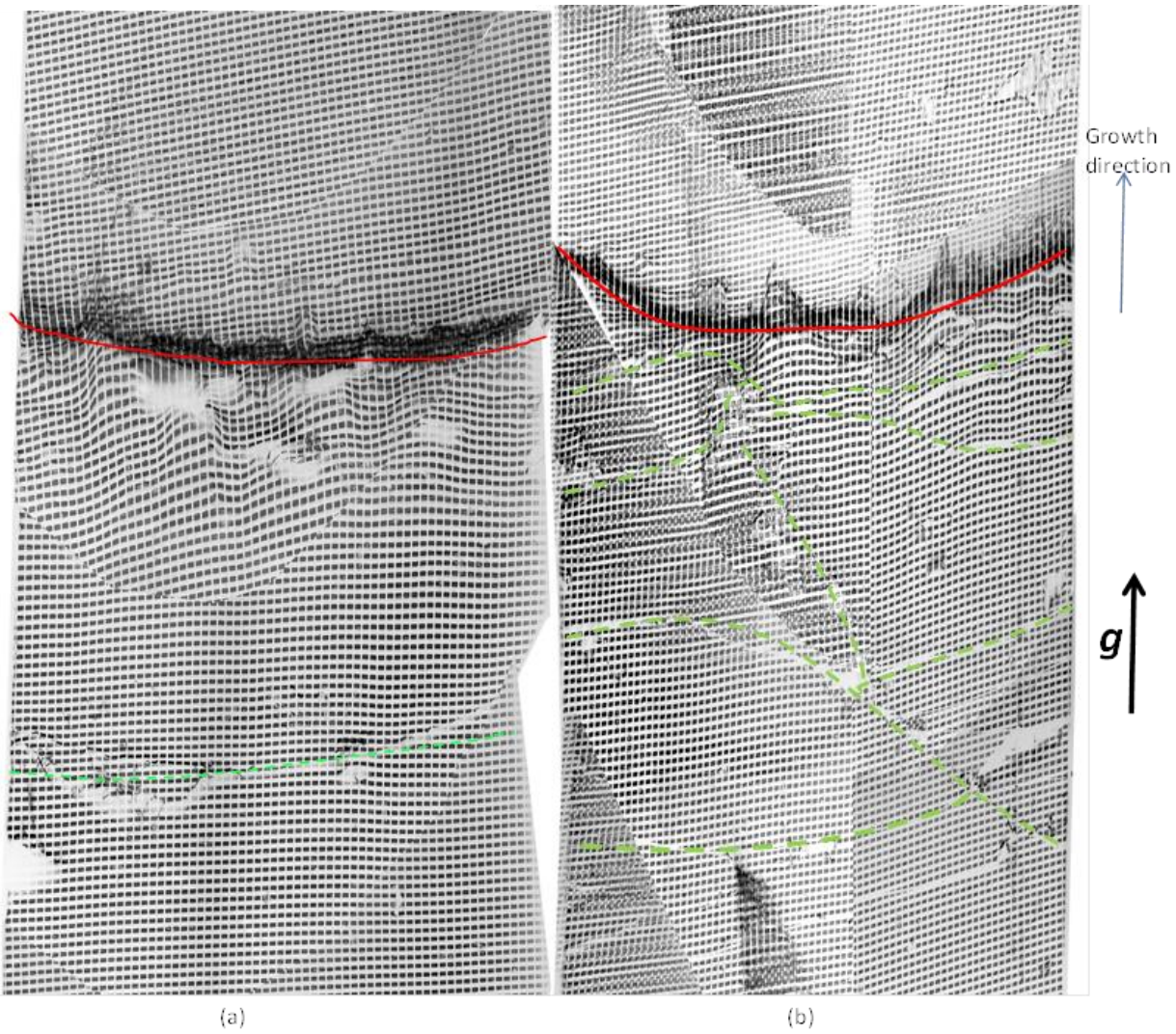

Figure 4.20. Significant distortion caused by boundary. (a), (b) are reticulograph images recorded from two side surface of a bulk sapphire sample

From the observation we can tell that all the grids before the significant boundary experience a relatively smooth expansion, then compressed abruptly along growth direction. According to the fundamental principle of stress mapping technique and the geometry relationship, the diffraction plane experiences a changing from smooth concave to a sharp twist and go back to perfect plane normal finally. The changing point from grids expansion to grids compression is the inflexion point of the plane function. After curvature analysis, we can tell the lattice parameter around the boundary regions defined by those atoms close to the wall is smaller than the stress free ones. The crystal shrinks at that boundary region.

b. Twin

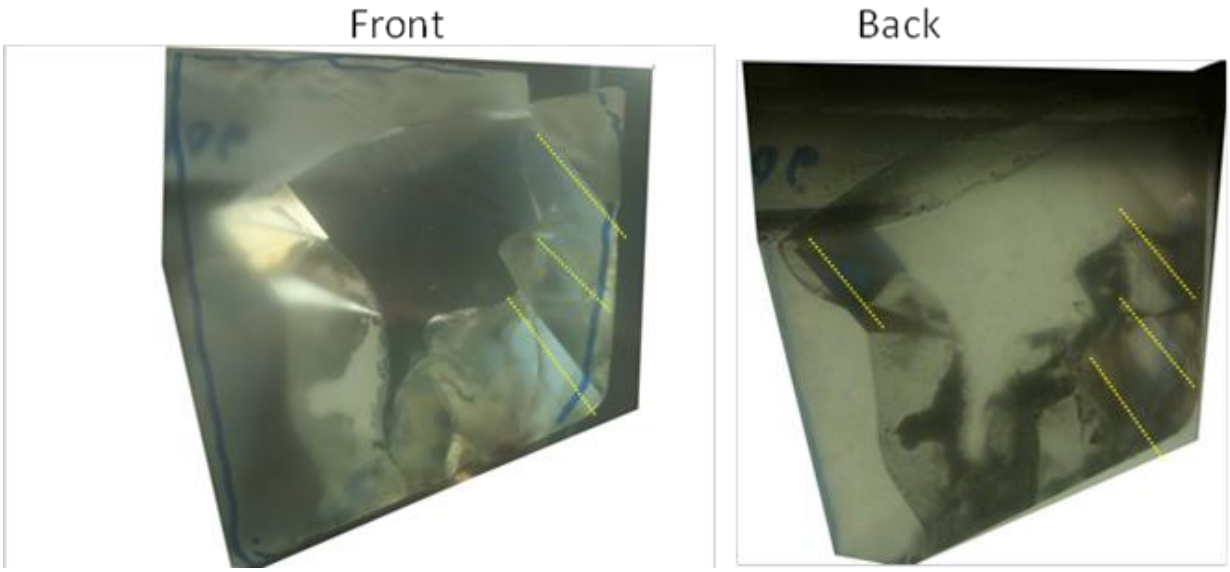

Figure 4.21. Optical images taken through polarizer showing the twins in the shoulder region of sample.

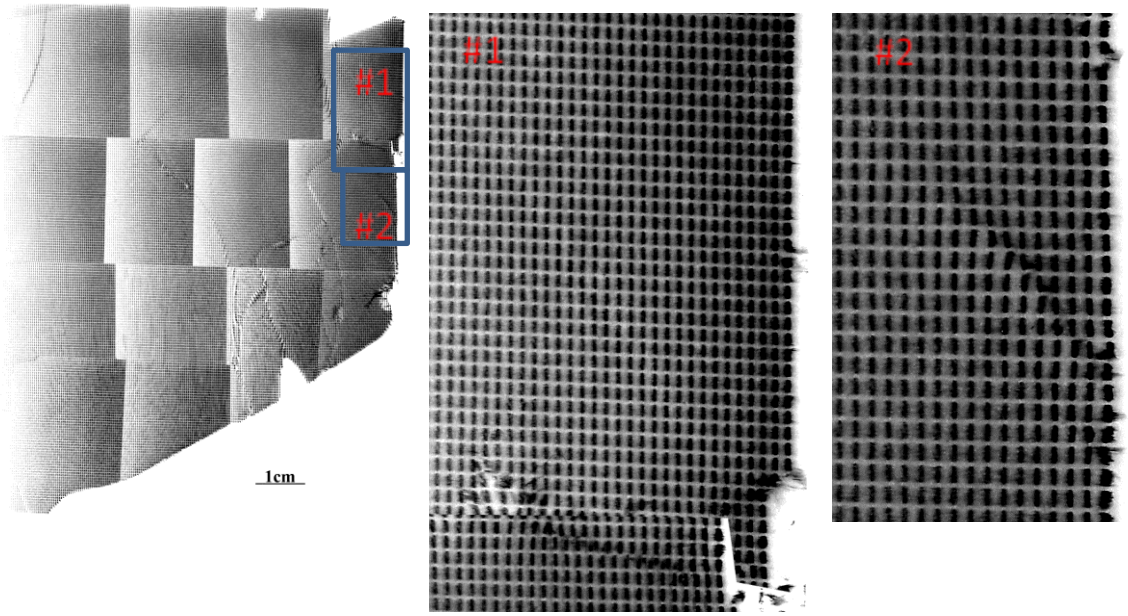

Figure 4.22. Reticulograph image of boule sample shoulder containing twins and cracks. Two twin regions are enlarged.

Until now, lots of twins associated with cracks are found in the sapphire samples. However, all of them are of rhombohedral type. A common phenomenon is, all the twins ends at the either at the surface or cracks, which implies the formation stage of twins are later than those formation stage of cracks. An example is given by optical image in Fig.4.21 (a), (b) of the front and back of one sample, the irregular surfaces are the cracks, the twins were marked with yellow dash lines. The rhombohedral twinning in sapphire is the only mode of plastic deformation under the

compressive stress along the c-axis at temperature below 1100°C, which indicates those cracks forms at higher temperature before that stage.

Twins intersecting the sample surfaces are normally weak in residual stress relative to boundaries and cracks. In Fig.4.22 (a), the distortion is even harder to tell. It might release the original stress to some extent. However, in fig. 4.22 (b), significant residual stress still exists around the twin area, and the comparable larger distortion near the crucible wall implies the origin of the twin.

c. Inclusion

Inclusions contamination could triggers cracks by producing large stress around the inclusion area. Fig. 4.23 shows the optical image of the seed full of cracks and an enlarged reticulograph image corresponding to that region. The yellow triangle shapes marked as the locations of inclusion could be easily observed. The yellow dash lines indicate the inclusions between the cracking surfaces. Significant distortion around those inclusion areas is noticed, which implies the origins of those cracks might be the stress as the result of inclusions.

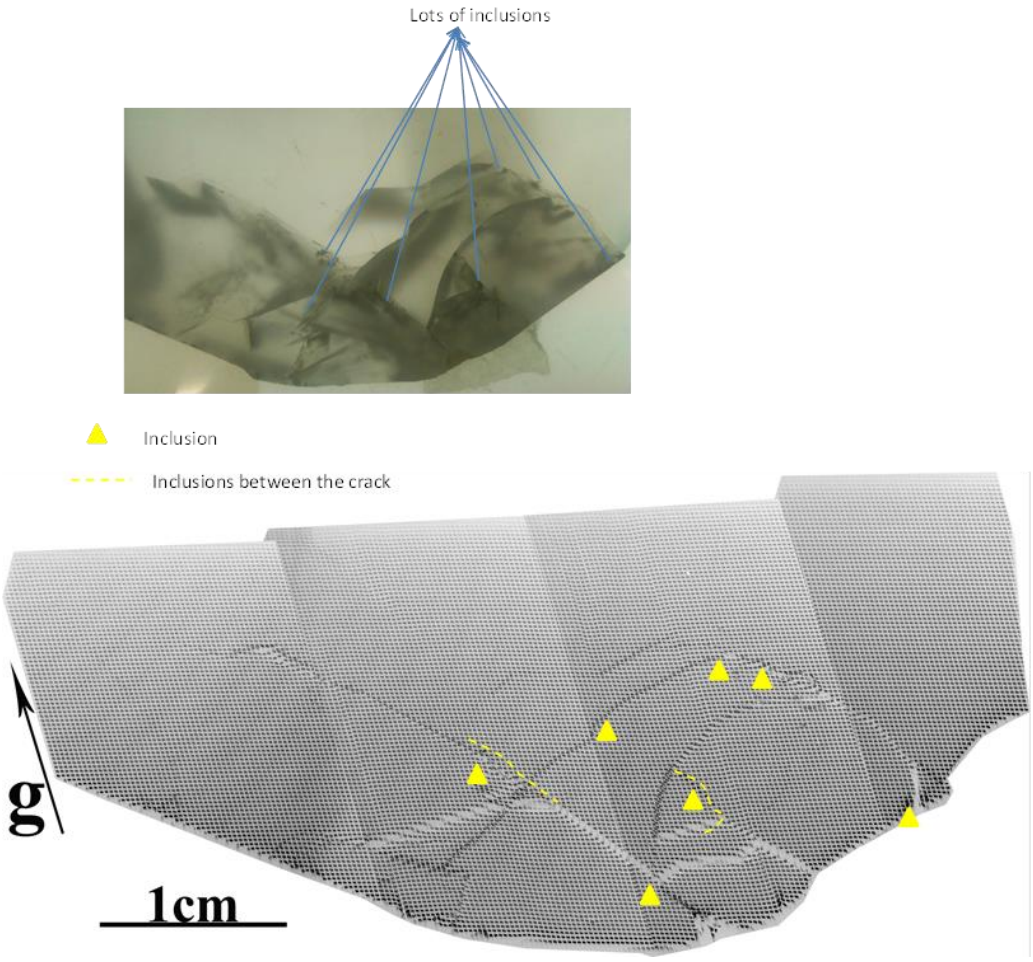

Figure 4.23. Optical and reticulograph image of the inclusion involving cracks in the bulk sample containing the seed.

Chapter 5. **Conclusions**

Issues studied in my work are mainly focused on types of defect in single sapphire crystal wafers, axial slices and bulks samples using X-ray topography technique as well as other characterization techniques. The defects structures, properties and forming mechanisms are studied in detail.

A) In sapphire wafer and axial slices samples, various linear and planar defects are studied. For dislocations, the dominant edge type basal plane dislocation which is frequently observed in sapphire is discussed. Burgers vector of helical dislocations in sapphire wafer is determined to be along a-direction and parallel to its axis after contrast analysis. Formation of this feature is due to the climbing and gliding of dislocation line with a screw component pinned at its two ends. A series of parallel dislocation loops observed might be the result of annihilation of two helices with opposite sign Burgers vectors. The Burgers vector for a special unfaulted dislocation loop is figured out to be along 1/3<10-11> by **g.b** analysis. The forming process of this feature can be due to a certain size of unstable fault created by the stacking sequence changes after inserting or removing two alumina/oxygen layers, is finally swept out by a shear. For planar defects, faceting and accumulation of dislocation mechanisms for boundary formation are investigated by topography analysis. The traditional etch pits method is also employed for revealing the property of individual dislocations. The morphology of etch pits in c-plane and m-plane wafer are discussed separately. The low angle boundary accumulated by dislocation process is also observed by this method as well.

B) In sapphire bulk materials, rhombohedral twinning mechanism as the result of a shear stress loading in twinning plane is studied. Symmetric operation between twin and matrix is confirmed by the designed experiment carried out in back reflection geometry. Structure model for this type of twin is simulated for further interpretation. X-ray reticulography based on X-ray topography is utilized for understanding the origins of cracks in the boule region by qualitative analyzing the residual stress through the stress-mapping-via-ray tracing method developed in our lab. In addition to cracks, defects such as twins and boundaries are also discussed whose forming mechanisms are proved to be stress involved.

References.

1. NIMSoffice, Corundum, http://en.wikipedia.org/wiki/File:Corundum.GIF, (18 April 2009)

2. E.R. Dobrovinskaya, et al., 2009, Sapphire: Material, Manufacturing, Applications, p. 55—57

3. A. Serra, D.J. Bacon, R.C. Pond, March 2002, "Twins as barriers to basal slip in hexagonal-closed-packed metals," Metallurgical and Materials Transactions A, vol. 33A, p. 809.

4. NIMSoffice, Corundum, http://en.wikipedia.org/wiki/File:Corundum.GIF, (18 April 2009)
5. G. D. Watkins, 1997, "Native defects and their interactions with impurities in silicon", MRS Symposium Proceedings, vol. 469, p. 139.

6. Daniel C. Harris, May 2004, "A Century of Sapphire Crystal Growth", Proceedings of the 10th DoD Electromagnetic Windows Symposium, p. 5—6

7. Aram Dulyan, Verneuil process diagram, http://en.wikipedia.org/wiki/Verneuil_process, (16 February 2006).

8. V. N. Kurlov, "Sapphire: Properties, Growth, and Applications", Encyclopedia of Materials: Science and Technology, p. 8259—8265

9. http://www.sdmaterials.com/crystal_growth_technologies.html

10. Mark S. Akselroda and Frank J. Brunib, December 2012, "Modern trends in crystal growth and new applications of sapphire", Journal of Crystal Growth, vol. 360, p. 134–145.

11. Chandra P. Khattak et al., 2003, "Growth of 15-Inch Diameter Sapphire Boules", Proceedings of SPIE, Vol. 5078, P. 30027—30033.

12. Xu Jianwei, et al., September 1998, "Growth of large-sized sapphire boules by temperature gradient technique (TGT)", Journal of Crystal Growth, vol. 193, Issue. 1–2, p. 123–126.

13. http://www.mt-berlin.com/frames_cryst/descriptions/sapphire.htm

14. Balaji Raghothamachar, et al., 2006, "Defect Analysis in Crystals Using X-ray Topography", Microscopy Research and Technique, vol. 69, p. 343–358.

15. A R Lang and A P W Makepeace, 1999, "Synchrotron x-ray reticulography: principles and applications", J. Phys. D: Appl. Phys., vol. 32A, p. 97–103.

16. D. Hull and D. J. Bacon, 2001, “Movement of Dislocations”, Introduction to Dislocation, p. 58, India: Reed Educational and Professional Publishing Ltd.

17. D. Hull and D. J. Bacon, 2001, “Dislocations in Other Crystal Structures”, Introduction to Dislocation, p. 107, India: Reed Educational and Professional Publishing Ltd.

18. D. Hull and D. J. Bacon, 2001, “Dislocations in Other Crystal Structures”, Introduction to Dislocation, p. 108, India: Reed Educational and Professional Publishing Ltd.

19. R. G. Vardiman, November 1971, “The Chemical Polishing and Etch Pitting of Sapphire”, J. Electrochem. Sot. : SOLID STATE SCIENCE, Vol. 118, No. 11, p1804—1809.

20. J. A. Chapion, M. A. Clemence, 1967, “Etch Pits in Flux-Grown Corundum”, Journal of Material Science 2, p.153—159.

21. L. A. Marnasina, et al., 1982, “Chemical Etching of Sapphire”, Crystal. Res.& Technol., p.365—371

22. NIU Xin-huan, et al., April 2006, “Dislocation of Cz-sapphire substrate for GaN growth by chemical etching method”, Trans. Nonferrous Met. SOC. China 16, p. 187 —191

23. D. Hull and D. J. Bacon, 2001, “DislocationArrays and Crystal Boundaries”, Introduction to Dislocation, p. 160, India: Reed Educational and Professional Publishing Ltd.

24. D. Hull and D. J. Bacon, 2001, “DislocationArrays and Crystal Boundaries”, Introduction to Dislocation, p. 161, India: Reed Educational and Professional Publishing Ltd.

25. D. Hull and D. J. Bacon, 2001, “Movement of Dislocations”, Introduction to Dislocation, p. 24, India: Reed Educational and Professional Publishing Ltd.

26. O. Ambacher, 1998, “Growth and applications of Group III-Nitrides”, J. Phys. D: Appl. Phys. 31, p. 2653-2710 25

27. Hurlbut, Cornelius S.; Klein, Cornelis, 1985, Manual of Mineralogy, 20th ed. 26

28. B. D. Cullity, 1977, Elements of X-ray Diffraction, p. 59—62.

29. John D. Clayton, 2009, Finite Deformation by Elasticity, Slip and Twinning: Atomic Considerations, Continuum Modeling, and Application, P. 274—277

30. M. A. Jaswon and D. B. Dove, 1956, “Twinning properties of lattice planes”, Acta. Cryst., vol.9, p. 621-626

31. Vishwanath Sarkar, 2011, “Residual Stress Determination in Transmission Geometry”, Defect characterization and stress analysis by white beam synchrotron X-ray topography in single crystal semiconducting materials, p. 29.

32. Vishwanath Sarkar, 2011, “Residual Stress Determination in Transmission Geometry”, Defect characterization and stress analysis by white beam synchrotron X-ray topography in single crystal semiconducting materials, p. 32.

33. Vishwanath Sarkar, 2011, “Residual Stress Determination in Transmission Geometry”, Defect characterization and stress analysis by white beam synchrotron X-ray topography in single crystal semiconducting materials, p. 29.

34. Vishwanath Sarkar, 2011, “Residual Stress Determination in Transmission Geometry”, Defect characterization and stress analysis by white beam synchrotron X-ray topography in single crystal semiconducting materials, p. 33.

35. Vishwanath Sarkar, 2011, “Residual Stress Determination in Transmission Geometry”, Defect characterization and stress analysis by white beam synchrotron X-ray topography in single crystal semiconducting materials, p. 20.

36. Vishwanath Sarkar, 2011, “Residual stress Mapping and Depth Profiling in Packaged Silicon Integrated Circuit Using White Beam Synchrotron X-ray Diffraction topography”, Defect characterization and stress analysis by white beam synchrotron X-ray topography in single crystal semiconducting materials, p. 67.